

# Logical discrimination of multiple disease-markers in an ultra-compact nano-pillar lab-in-a-photonic-crystal

Cite as: J. Appl. Phys. **126**, 234701 (2019); <https://doi.org/10.1063/1.5100681>

Submitted: 19 April 2019 . Accepted: 19 November 2019 . Published Online: 16 December 2019

Abdullah Al-Rashid , and Sajeev John



View Online



Export Citation



CrossMark

## Lock-in Amplifiers up to 600 MHz



Zurich  
Instruments



# Logical discrimination of multiple disease-markers in an ultra-compact nano-pillar lab-in-a-photonic-crystal

Cite as: J. Appl. Phys. 126, 234701 (2019); doi: 10.1063/1.5100681

Submitted: 19 April 2019 · Accepted: 19 November 2019 ·

Published Online: 16 December 2019



View Online



Export Citation



CrossMark

Abdullah Al-Rashid<sup>a)</sup>  and Sajeew John<sup>b)</sup>

## AFFILIATIONS

Department of Physics, University of Toronto, 60 St. George St., Toronto, Ontario M5S 1A7, Canada

<sup>a)</sup>Electronic mail: [abdullah.alrashid@utoronto.ca](mailto:abdullah.alrashid@utoronto.ca)

<sup>b)</sup>Electronic mail: [john@physics.utoronto.ca](mailto:john@physics.utoronto.ca). URL: <http://www.physics.utoronto.ca/~john/>

## ABSTRACT

We present a theoretical prescription for a physically realizable Lab-in-a-Photon-Crystal optical biosensor that can instantaneously detect and discriminate multiple analytes, both quantitatively and combinatorially, in a single spectroscopic measurement. Unlike other biosensors that utilize simple resonance modes, our fundamental operating principle is the analyte-induced hybridization of waveguide modes and surface modes in a photonic bandgap, leading to a complex spectral fingerprint. Our real-world liquid-infiltrated photonic crystal sensor supplants two-dimensional conceptual paradigms proposed earlier with realistic features and a path to implementation. A square-lattice photonic crystal of nanopillars with fixed height but differentiated cross sections within a narrow flow-channel is used for cascaded transmission of light through the photonic bandgap. The nanopillar array is placed on a thin layer of high-refractive-index backing material resting on a glass substrate with fluid and biomarker flow along the waveguide direction. Using finite-difference time-domain simulations of light transmission perpendicular to the waveguide, a variety of spectral fingerprints are identified as various disease-marker combinations bind to specific lines of nanopillars. Various diseases or various stages of a given disease are detected and differentiated through the interplay of central-waveguide resonances with edge modes and three-dimensional index-guided bulk modes. This offers a distinctive mechanism for instantaneous disease diagnosis using a minimal volume of fluid sample.

Published under license by AIP Publishing. <https://doi.org/10.1063/1.5100681>

## I. INTRODUCTION

Detection and monitoring of early-stage disease-markers from body tissue and fluid samples instantly and *in situ* using a millimeter to centimeter-scale optical chip—without recourse to time-consuming and expensive external laboratory testing—is one of the holy grails of medical diagnostics. In this article, we present the detailed design of a Lab-in-a-Photon-Crystal (LiPC) for optical biosensing to provide a rapid and simple means for point-of-care medical diagnostics. Using optical modes that extend over large expanses of the fluid fraction of the device, different concentrations of multiple disease-markers can be distinguished in a single measurement, leading to better diagnostic performance compared to conventional biosensors.

Photonic crystals (PCs)<sup>1,2</sup> are artificial dielectric materials with periodic variations at a scale of roughly half the wavelength of light. Suitably engineered PCs completely inhibit the propagation of light

within them over a range of frequencies known as the photonic bandgap (PBG). PBGs offer “blank slates” for engineering optical modes, which can be tailored for specific sensing applications without being obfuscated by spectral collisions with spurious modes. Defects due to local deviations from periodicity in a PC admit optical modes disallowed by the PBG of the bulk material.<sup>3</sup> Common examples are *line-defect waveguide modes* hosted by lines of altered unit-cells and *surface modes*<sup>4</sup> at truncated interfaces of a PC with another material. Unlike index-guiding, where total internal reflection confines light into high-index media with only evanescent leakage into low-index surroundings, PC defect modes can concentrate light directly into low-index regions of interest. This is significant for optical biosensing, which typically involves the detection of low-index biological materials via illumination within a high-index sensing structure. It is well-known that both high optical field concentration in the *analyte* region and high-quality

factors are necessary for biosensing with high sensitivity and a low limit-of-detection. While these two requirements can be in mutual conflict for many conventional biosensors, PCs offer a means of achieving both.

Our nanopillar design provides a physical embodiment and enhancement of the two-dimensional (2D) conceptual paradigm presented earlier.<sup>5</sup> In our biosensing mechanism, analyte-induced changes in coupling between a PBG-waveguide mode, surface modes, and index-guided bulk modes provide a detailed spectral fingerprint responsive to the presence of multiple analytes. This detailed fingerprint consists of frequency-shifts of optical resonances due to analyte-binding and novel spectral features arising from hybridization of multiple optical resonances.

In previous designs,<sup>6–8</sup> the detection of multiple disease-markers is achieved by a series array of biosensors on a large chip with each individual sensor assigned to a single marker. Moreover, each sensor consists of a PC point-defect that supports a single optical resonance mode. Our LiPC introduces two major improvements to multiplexed biosensing. First, it judiciously places multiple optical resonances into a single sensing region. This enables optical resonances to couple with each other (*mode-hybridization*), depending on their spatial and spectral proximity, leading to a complex spectral fingerprint that appears in the transmission intensity vs frequency. This is markedly different from the use of spatially-separated optical modes, each with a Lorentzian transmission line shape. In our LiPC, multiplexed biorecognition occurs in a much smaller device volume, requiring a much smaller sample volume. Second, the spatial profile of our optical sensing modes offers an important advantage over previous works. Unlike the point-defect modes utilized elsewhere,<sup>6–9</sup> ours are extended waveguide modes that are functionalized to capture disease-markers throughout the biosensing chip. This relatively broader “net” for capture implies that disease-markers have a shorter distance to diffuse before being detected, thereby reducing the time required for diagnosis.

In the prior literature, PC defect structures, with their light-localizing properties, have formed the basis of numerous optical biosensors.<sup>9–12</sup> While these single-mode sensors harness light-concentrating properties of one PC defect, the full sensing potential afforded by multiple, optically-coupled modes has remained largely unexplored. Other approaches to optical biosensing include surface plasmon resonance (SPR) sensors,<sup>13</sup> whose primary drawbacks consist of the inherently lossy nature of SPRs. Lossless dielectric metamaterial membranes have also been considered for sensing<sup>14</sup> but, like SPR sensors, they probe the analyte using only an evanescent field. There are also sensors based on gratings<sup>15</sup> and waveguides,<sup>11,16</sup> exploiting changes to resonant modes due to refractive index changes introduced by the presence of the analyte. Instances of grating-coupled waveguide sensors, such as Optical Waveguide Light-mode Sensors (OWLS),<sup>17–19</sup> have also been encountered. In comparison, our work employs a dual-grating sandwiching a central-waveguide embedded in the PBG material. Light couples to the structure through the proximal (i.e., near-to-source) grating, followed by an interaction with the central-waveguide mode, before exiting the system via the distal (i.e., far-from-source) grating. Unlike most of the SPR, metamaterial, waveguide, and grating sensors, our system is capable of multiparametric detection.

Recently, the use of a multimode waveguide for multiparametric detection has been reported in the literature,<sup>16</sup> with the drawback that fluorescent labeling of the analytes is necessary. In comparison, our design is immanently label-free. As mentioned earlier, multiparametric biosensing based on frequency-shifts of multiple, mutually-independent resonances<sup>6–8</sup> has also been demonstrated through a series of cavity-waveguide interactions in a PC background. Such systems can sometimes suffer from spectral “cluttering” due to spurious optical modes and seem to offer no means of self-calibrating background fluid indices. Our LiPC overcomes the first issue by the use of *optically-coupled* modes, which undergo *transmittance-level modulations* in addition to frequency-shifts in response to the presence of analytes. Thus, a collision of modes in frequency space helps shape the spectral fingerprint for unambiguous detection. This can be extended to feature a larger number of analytes by using multimode surface and waveguide structures.<sup>20</sup> Furthermore, we offer calibration of background fluid index via optical modes specific to our LiPC design.

## II. DESIGN OVERVIEW

Detection of bulk fluid refractive index changes<sup>21–23</sup> in practical biological samples like blood plasma is often insufficient for specific diagnosis. Considering three plasma components albumin, fibrinogen, and  $\gamma$ -immunoglobulin, many combinations of their concentration changes can lead to the same bulk index change, yet indicate a wide variety of disorders. Therefore, we opt for a design based on *biorecognition*, which precipitates diagnostically-relevant factors out of solution and immobilizes them in designated regions illuminated strongly by the engineered PC modes.

Our analyte-binding model constitutes thickness increments of  $n = 1.45$  material isolated from a biofluid background with  $n = 1.35$ . These values are reasonable experimental estimates from adsorbed layers of fibrinogen, lysozyme,  $\gamma$ -immunoglobulin, and albumin.<sup>24</sup> Biorecognition may be accomplished through the complementary binding of biological substances, such as antibodies and antigens or proteins and DNA aptamers.<sup>25,26</sup> Once biorecognition occurs in our LiPC, optical properties of individual modes and their associated couplings change, leading to detailed spectral fingerprints.

Moreover, our LiPC design extends the functionalities of its pure 2D predecessor<sup>5</sup> by providing an additional mode which is sensitive to changes of bulk refractive index in the fluid. This mode may be used for sensor calibration for situations where the presence of undesirable impurities may render  $n \neq 1.35$  for the fluid background. This is one way our design accounts for measurement noise from biological sources. Furthermore, to account for other forms of biological noise, such as nonspecific absorption leading to false positive or false negative diagnoses, the sensor can be calibrated for a variety of analyte refractive indices  $n \neq 1.45$ , as demonstrated for its predecessor.<sup>5</sup> We also point out that our sensor does not aim to achieve extreme values for sensitivity or Q-factors of optical modes. Instead, we focus on eliminating the usual trade-off between these two performance indicators.<sup>5</sup> By eliminating the need for oversensitivity using detailed spectral signatures derived from mode-hybridization, amplification of measurement noise is mitigated.

Furthermore, PCs can be designed to admit large flow channels—both at the surfaces and within the interior of the chip. Fluid flow through PCs for the purpose of sensing has been treated in the previous literature.<sup>27,28</sup>

The PBG plays a significant role in our design, allowing a sufficient free spectral range (FSR) for the LiPC modes to be “uncluttered” in frequency space due to the absence of other spurious modes, which may be accessible by improper beam collimation, disorder-induced scattering, etc. Furthermore, transmission-level modulations brought about by the hybridization of LiPC modes enable our sensor to make unambiguous measurements even when these modes may collide in frequency. We utilize a square lattice of pillars with square cross section, as this is known to provide a large 2D PBG compared to other lattice structures and cross-sectional shapes.

We depict our LiPC design in Fig. 1. Glass ( $n = 1.5$ ) forms the base of this structure and is considered to extend infinitely beneath the device. There is a thin layer of high-index dielectric backing material ( $n = 3.4$ ) above the glass. On top of this backing layer, a 2D square lattice of square nanopillars forms the active region of the LiPC. In terms of the unit-cell side-length  $a$  of the square 2D PC progenitor,<sup>5</sup> the backing layer has a thickness of  $b/a = 0.2$  and the nanopillars have a height  $d/a = 3.0$ . Glass walls

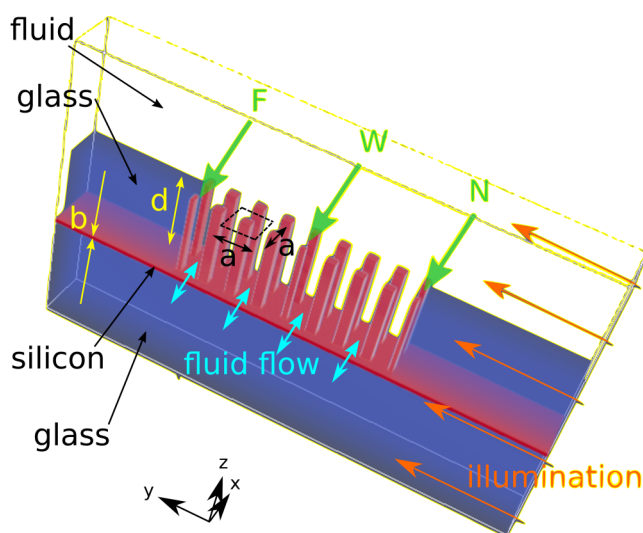


**FIG. 1.** A glimpse of the final design for the LiPC. The structure, consisting of silicon nanopillars ( $n = 3.4$ ), is a protrusion of the 2D system designed previously<sup>5</sup> over a height  $d$  from a high-index backing material of depth  $b$ , which in turn lies on a glass substrate ( $n = 1.5$ ). The sidewalls of the flow channel are also made of glass. Silicon regions are shown in red and glass regions in blue, with fluid regions in the outlined computational domain left colorless. The 2D PC used as the basis for the design has a square lattice and a square unit-cell of size  $a \times a$ . The system is open to fluid from the top and repeats periodically in the fluid-flow direction. Nanopillars form the skeleton for a connected set of spaces for fluid-infiltration. Analyte may bind to three sites: the near-to-source surface grating  $N$ , the central waveguide  $W$ , and the far-from-source surface grating  $F$ .

with a height of  $d$  encase LiPC along the direction of periodicity and form a channel for guiding the flow of fluid containing bio-markers. For clarity, the three directions  $x$ ,  $y$ , and  $z$  are often referred to as *fluid-flow direction*, *light propagation direction*, and *vertical direction*, respectively. The structure is periodic in the direction of fluid-flow, with a single period shown in Fig. 1. The system is illuminated from one side along the light propagation direction, with transmission measurements taken on the other side.

The feasibility of experimentally realizing high-quality optical resonances in a nanopillar array for the purpose of sensing has been demonstrated previously,<sup>23</sup> with the usual trade-off between quality factor and measurement sensitivity for a single optical microcavity graphically illustrated as a function of nanopillar height. Our design extends this approach to multiple, coupled optical modes, resulting in more detailed spectral fingerprints that can distinguish and discriminate multiple disease-markers with a single optical measurement.

The LiPC structure depicted in Fig. 1 has a large fluid region ( $n = 1.35$ ) above the trough containing nanopillars. We refer to this as an *open-top design*, into which samples can be dropped from above. The open-top design simplifies fluid-flow within the LiPC and reduces the possibility of clogging by large impurities in a fluid sample. Practically, our structure, with foreseeable nanopillar heights on the order of  $1\text{--}5\ \mu\text{m}$ , might be submerged by the fluid with height of the order of  $10\text{--}30\ \mu\text{m}$ , and then be capped by a glass ceiling to prevent spillage. The final capping would facilitate the generation of flow pressure through the device. The capping, however, would be sufficiently high to not affect the optics. Another benefit from the open-top design occurs when a cap of analyte binds to the top surfaces of the nanopillars. In addition to binding at the side-surfaces, this top-surface binding can be detected by evanescent light that extends from the sensor into the fluid environment above.

We provide geometric details of the structure in Fig. 2. The unit-cell of our LiPC, shown in Fig. 2(a), is a 2D square lattice of dielectric nanopillars ( $n = 3.4$ ; red region). Nanopillars of dimensions  $w \times w \times d$  stand on a thin layer of the same material with thickness  $b$  while being immersed in a fluid background ( $n = 1.35$ ; beige region inset and clear foreground regions), forming a three-dimensional (3D) unit-cell of 2D periodicity  $a \times a$ . The maximal 2D PBG for this configuration is obtained for  $w = 0.4 \times a$ , providing the geometric dimension for the intrinsic PC to be used in the subsequent design. Figure 2(b) displays a top view of our LiPC, which resembles the 2D conceptual paradigm.<sup>5</sup> This features an engineered PC (red and white regions) with  $w = 0.4 \times a$  and endowed with other features. The nanopillar PC is placed within a fluid-flow trough of glass ( $n = 1.5$ ; blue region in Fig. 1) with walls at the extremities of the light propagation direction ( $y$ -direction). A central-waveguide line-defect is created in the intrinsic PC by using a modified square of side-length  $w_{wg} = 0.25 \times a$ . Moreover, the extremal PC unit-cells are modified by an encroachment of glass by a proportion  $\tau = 0.5$  of the unit-cell length  $a$  [Fig. 2(c)]. This creates surface modes at both termini of the structure in the light propagation direction. We refer to the glass-infringed terminal layers as *surface gratings*. Moreover, the structure is *period-doubled* along the fluid-flow direction ( $x$ -direction) by the addition of a small perturbation

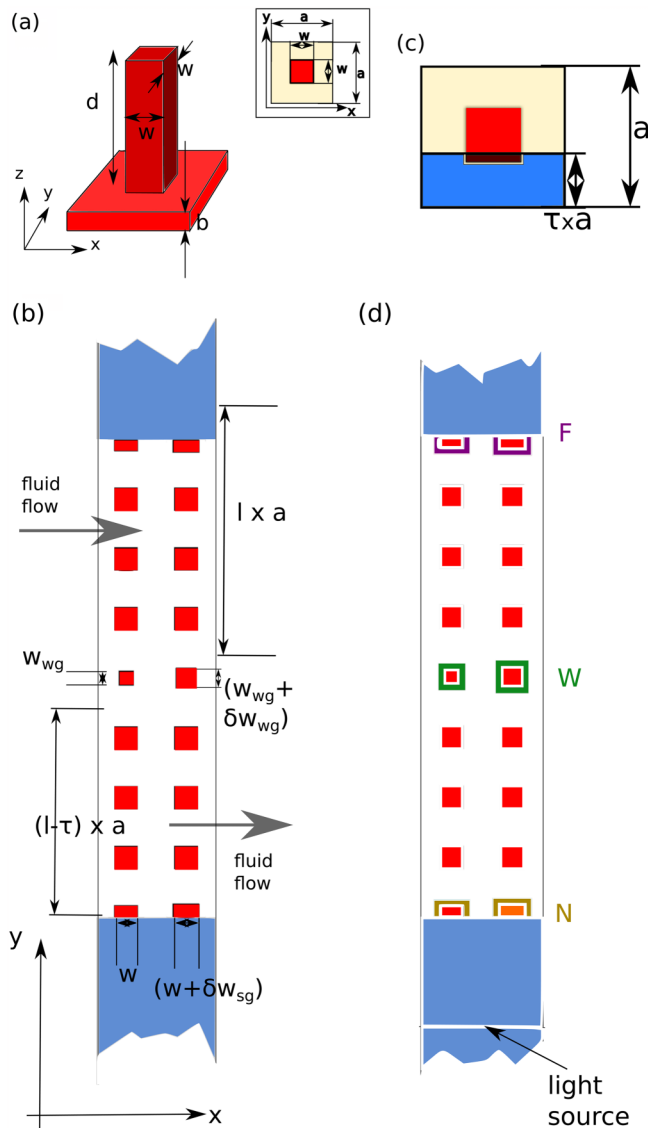


**FIG. 2.** Details on the geometry of the final design. (a) Unit-cell for the underlying architecture used for the proposed design (foreground illustration not to scale): dark shading indicates solid, high-refractive-index material and light shading indicates fluid background. The choice of  $w/a = 0.40$  provides an optimum 2D PBG. The 2D PC unit-cell (inset) is protruded by a length of  $d$  along the  $z$ -direction to create a nanopillar structure from a thin layer of a high-index material with thickness  $b$ . For the final design,  $d/a = 3.0$  and  $b/a = 0.2$ . (b) Annotation of the dimensions used: The nanopillar array is periodic along the  $x$ -direction and truncated by the infinite glass material along the  $y$ -direction. In our ideal device, we choose  $w/a = 0.40$ ,  $w_{wg}/a = 0.25$ ,  $\delta w_{wg}/a = 0.10$ , and  $\delta w_{sg}/a = 0.05$ . (c) Illustration of the concept of the truncation parameter  $\tau$  at the terminations: the parameter  $\tau = 0.50$  denotes the proportion of the PC unit-cell encroached upon by the terminating glass material. (d) Analyte-binding regions: analyte may bind to a combination of three distinct sites, namely, the near-to-source surface grating ( $N$ ), the central-waveguide region ( $W$ ), and the far-from-source surface grating ( $F$ ). In an earlier work on a 2D paradigm,<sup>5</sup> location  $N$  was referred to as  $B$  and  $F$  as  $T$ .

$\delta w_{wg} = 0.10 \times a$  to the central-waveguide block as well as a perturbation  $\delta w_{sg} = 0.05 \times a$  to the surface gratings. This is crucial to ensuring that the surface modes lie above the *light line* in a photonic band diagram in order for light to be able to couple to them from the glass outside.<sup>5</sup> There are three standalone regions which break the translational symmetry of the 2D PC in Fig. 2(d): namely, the two surface gratings  $N$  and  $F$ , as well as the waveguide  $W$ . These regions are also illustrated in Fig. 1 and admit localized (in the  $y$ -direction) optical modes, which can be used for interrogating the presence of the analyte at these locations.

The coupling of light in and out of the nanopillar region may be accomplished using small-mode-area photonic crystal fibers (PCFs) channeling light along the light propagation direction. These PCFs could couple light to the sidewalls of the fluid-flow trench. In this arrangement, the finite-height glass walls with a thin silicon backing layer can act as a waveguide to deliver incoming light from the illuminating PCF to the nanopillar region, as well as to deliver outgoing light to an output PCF.

The structure in Fig. 1 is optimized based on two criteria: (i) optical properties for analyte detection and (ii) structural robustness and stability. Details of the design process have been relegated to Appendixes A, B, and C for brevity. It is demonstrated below that our structure is capable of differentiating between all eight possible combinations of analyte-binding scenarios pertinent to three distinct analytes. This is a notable improvement over the six cases distinguishable by its predecessor.<sup>5</sup>

We envision the fabrication of our LiPC shown in Fig. 1 to start from a glass substrate with a layer of high-index dielectric ( $n = 3.4$ ) of thickness  $b/a = 0.2$  followed by a layer of glass with thickness  $d = 3.0 \times a$  on top. A flow-channel can then be etched into the top glass layer within which the nanopillar array of the LiPC will also be housed. The high-index dielectric nanopillar array with precisely defined dimensions can then be grown within the open channel by various techniques.<sup>29–31</sup> A particularly useful approach for achieving differentiated and precise nanopillars is by growth through a lithographically-patterned photoresist.<sup>32</sup> Furthermore, a final challenge is to functionalize the analyte-binding surfaces with high-resolution 3D ink-jet printing.<sup>33,34</sup> This functionalization occurs along lines that run along the central waveguide (denoted  $W$  in Fig. 1), the near surface grating ( $N$ ) and the far surface grating ( $F$ )—with surface gratings labeled near or far from the optical source. The process may be aided by masking those areas outside the desired lines during the printing process. Once the surface gratings and central waveguide have been functionalized, it would be impossible to subject the structure to high-heat and/or complicated chemical treatment processes without damaging the delicate materials involved.

To provide concrete values for physical dimensions for the device in Fig. 1, we consider two possible optical wavelengths of operation. For the first example wavelength  $\lambda_0 = 1.5 \mu\text{m}$ , using a normalized frequency  $a/\lambda_0 \approx 0.290$  (approximate median of normalized frequencies from FDTD spectra presented later in Figs. 8–14), the PC unit-cell side-length becomes  $a \approx 435 \text{ nm}$ , with PC nanopillars having a height of  $d = 3.0 \times a \approx 1.3 \mu\text{m}$  and side-lengths  $w = 0.4 \times a \approx 175 \text{ nm}$ . Similarly, for  $\lambda_0 = 5 \mu\text{m}$ ,  $a \approx 1.45 \mu\text{m}$ ,  $d \approx 4.35 \mu\text{m}$ , and  $w \approx 580 \text{ nm}$ .

### III. SPECTRAL FINGERPRINTS OF BIOMARKER COMBINATIONS

We now characterize the sensing properties of our short-pillar LiPC which improves upon the sensing characteristics of its pure 2D counterpart. As a starting point, we benchmark the spectral response from our sensor against results from the 2D progenitor.<sup>5</sup> Biosensor operation is simulated using the Finite-Difference Time-Domain (FDTD) method for solving Maxwell's equations using the open source *Meep* library.<sup>35</sup> As indicated earlier, we measure lengths in terms of the PC unit-cell side-length  $a$  and use 10 FDTD mesh points for every unit of length. The standard method of defining geometries in *Meep* was modified by an  $\epsilon$ -averaging scheme to keep the computations tractable. Details are provided in Appendix D. Once again, analyte-binding is possible at three different locations: the surface grating near the optical source ( $N$ ), the central-waveguide region ( $W$ ), and the surface grating far from the optical source ( $F$ ). We use the abbreviated location designations as labels for analyte-binding configuration: e.g.,  $WN/WF$  denotes analyte-binding at the waveguide region in addition to one of the surface gratings. For both the LiPC and its 2D progenitor, a total of eight different analyte-binding configurations are possible. Beyond the exit grating  $F$ , thin-silver detectors are placed at various locations along the vertical direction to capture optical transmission signals when the system is illuminated from beyond the entry grating  $N$ . These detectors are labeled as 00, 01, 02, 03, 04 in correspondence to their vertical levels, as shown in Fig. 3.

Before discussing the unique spectral behavior of our real-world LiPC, we review the optical modes of the 2D paradigm.<sup>5</sup> Based on the selected width of the fluid flow channel, three hybridized optical modes emerge from the combination of these standalone optical modes sustained at the surface gratings  $N$  and  $F$  and

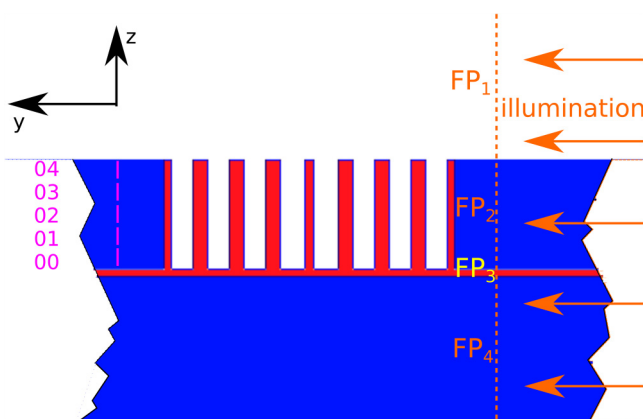


**FIG. 3.** FDTD detector setup for LiPC simulations. The power flux of the light illuminating the system is calculated over a flux plane with nonuniform index.  $FP_1$  has  $n = 1.35$ ,  $FP_2$  has  $n = 1.5$ ,  $FP_3$  has  $n = 3.4$ , and  $FP_4$  has  $n = 1.5$ . Five thin-silver transmission detectors labeled by 00, 01, 02, 03, and 04 (in order of increasing  $z$ -level) are placed at various locations. These silver detectors span the  $x$ -direction of the geometry and provide information on the  $z$ -variation of the transmittance. Details of power flux and transmittance calculations are provided in Appendix A.

the central waveguide  $W$ . The standalone (i.e., unhybridized) optical modes at  $N$  and  $F$  are degenerate in frequency, while the one at  $W$  is close in frequency to the former but unequal. Given the finite extent of the 2D-PC in the  $y$ -direction, this allows for the standalone modes to interact and hybridize via evanescent tunneling through the 2D-PC. From the mathematical discussion presented earlier,<sup>5</sup> there are three hybridized modes of the 2D prototype relevant to biosensing. Two are surfacelike modes (SLMs), one of them is an exact antisymmetric linear combination of the surface modes at  $N$  and  $F$ , while the other is an approximately symmetric linear combination of the same modes with some mixture of the waveguide mode at  $W$ . The third optical mode is a wavelike mode (WLM), principally composed of the central waveguide mode about  $W$ , with small contributions from the modes at  $N$  and  $F$ . SLMs are visualized in Fig. 4 and WLM in Fig. 5. Due to the *finite* size of the nanopillars in the third dimension, index-guided fields may also reside in the intrinsic portion of the PBG material (which is the *defect-free* 2D-PC regions extended into the  $z$ -direction, or alternatively, nanopillar regions other than the analyte-binding sites  $N$ ,  $W$ , and  $F$ ). We refer to them as Index-Guided Bulk Modes (IGBMs). IGBMs are not possible in a perfect 2D system and disappear in the limit of  $d \rightarrow \infty$ . IGBM fields are presented in Figs. 6 and 7. Briefly, the sensing modes of the final structure are determined by a two-step process: (i) index-confinement of the SLMs and WLM of the 2D progenitor<sup>5</sup> along the vertical direction without the presence of a high-index backing layer and (ii) selection of the shortest possible nanopillar heights using a high-index backing layer for greater structural stability without compromising sensing properties. Details of step (i) are in Appendixes A and B, while step (ii) details are in Appendix C.

We note that the values of  $d$  and  $b$  that enable the best biosensing functionality are very specific. For  $b/a \neq 0$  cases, the value of  $d/a = 3.0$ , which is exactly *half* of the value for unbacked LiPC design in Appendix A, exhibits electric field patterns very close to the optimal level of index-confinement along the vertical direction. Figure 4 contains the SLM field patterns for the high-index-backed LiPC. The  $xy$ -slices of the fields closely resemble those of the long-pillar sensor in Appendix B. Fields in the  $yz$ -slices of the backed, short-pillar LiPC also correspond well with the upper half of the those for the unbacked, long-pillar case. We also compare WLM field distributions for the backed, short-pillar LiPC in Fig. 5 with those of the unbacked, long-pillar sensor in Appendix B. The same halving of the field patterns appears with the appropriate choice of high-index backing layer. Similar observations are made for IGBM1 in Fig. 6.

For completeness, we include the field pattern of a higher-order index-guided bulk mode—labeled IGBM2—for the short-pillar LiPC in Fig. 7. IGBM2 occurs at a higher frequency than IGBM1, the SLMs, and WLM.

Before progressing further, we tabulate various acronyms introduced into Table I for the reader's convenience.

Figures 8–14 present spectral fingerprints for the seven analyte-binding cases  $\{W, N, WN, F, WF, NF, WNF\}$ , where analyte is bound to at least one of the binding sites in the short nanopillar LiPC. We increment the analyte thickness progressively by an amount  $\Delta t^{(\text{min};\text{FDTD})}$ . Specifically,  $\Delta t^{(\text{min};\text{FDTD})} = 0.05 \times a$  represents *half* the distance between consecutive FDTD mesh points and provides an FDTD-based upper-bound estimate for the limit-of-detection.

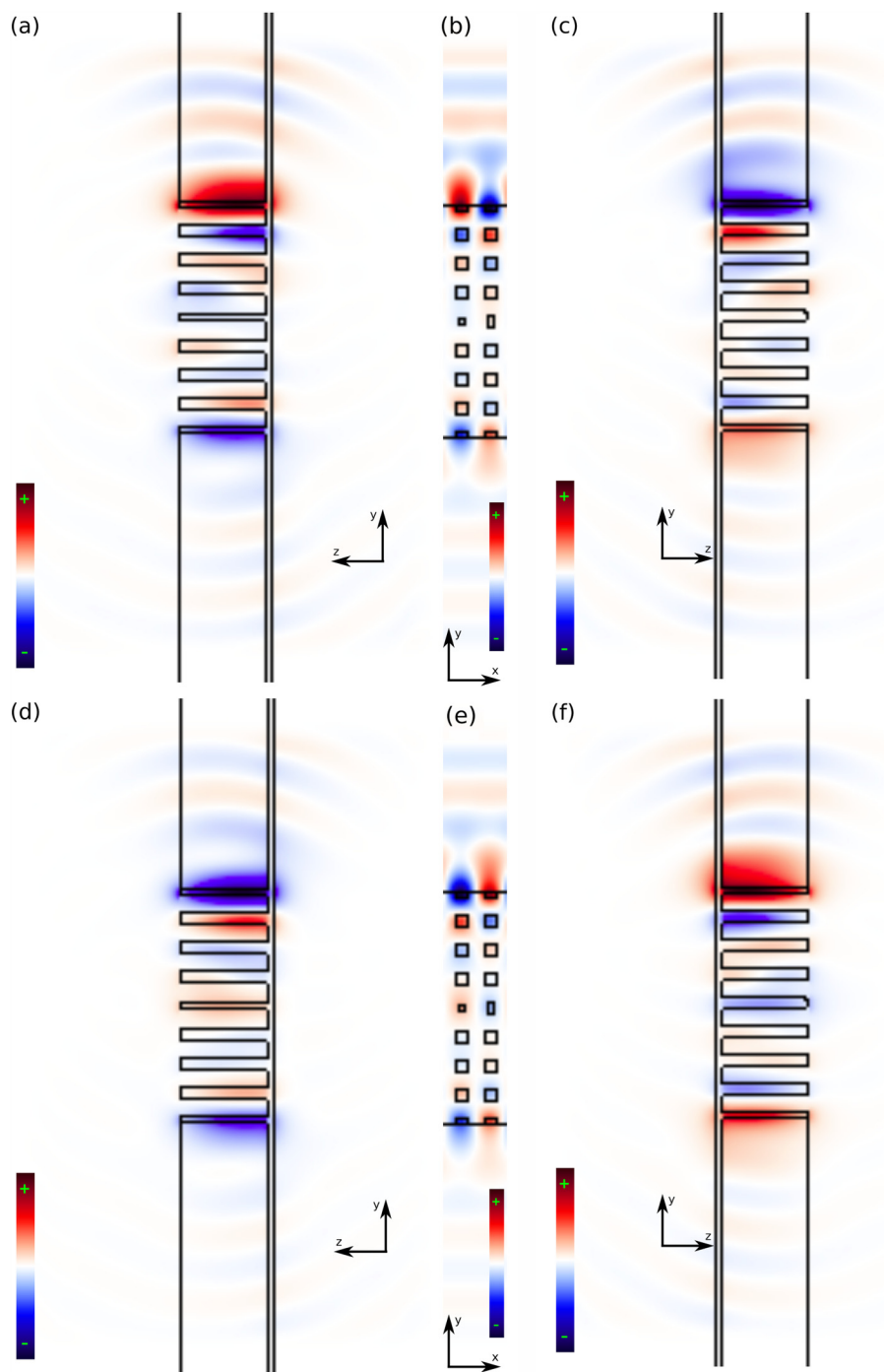


**FIG. 4.** SLM electric field [ $\Re(E_z)$ ] snapshots for backed, short-pillar LiPC. Two distinct cases are observed—antisymmetric [(a)–(c)] and symmetric [(d)–(f)]; the former admits no field contribution from the waveguide, while the latter does: (a) profile (yz-slice) of antisymmetric case along centerline of left unit-cell of x-period-doubling, (b) overview (xy-slice) of antisymmetric case at plane through nanopillar z-centers, (c) profile (yz-slice) of antisymmetric case along centerline of right unit-cell of x-period-doubling, (d) profile (yz-slice) of symmetric case along centerline of left unit-cell of x-period-doubling, (e) overview (xy-slice) of symmetric case at plane through nanopillar z-centers, and (f) profile (yz-slice) of symmetric case along centerline of right unit-cell of x-period-doubling.

Due to the averaging scheme presented in Appendix D such that each FDTD mesh point represents an averaged  $\epsilon$  taken over a finer subgrid interspersed within its surroundings, our FDTD setup is able to resolve analyte thickness changes that fall below the FDTD mesh size. Transmittance is calculated for five different detection

locations as depicted in Fig. 3. Notable transmission peaks in Figs. 8–14, in order of increasing frequency, correspond to IGBM1, SLMs, and WLM, respectively. For the LiPC spectral behaviors illustrated in Figs. 8–14, we include the corresponding 2D system's reference spectrum in a subfigure.

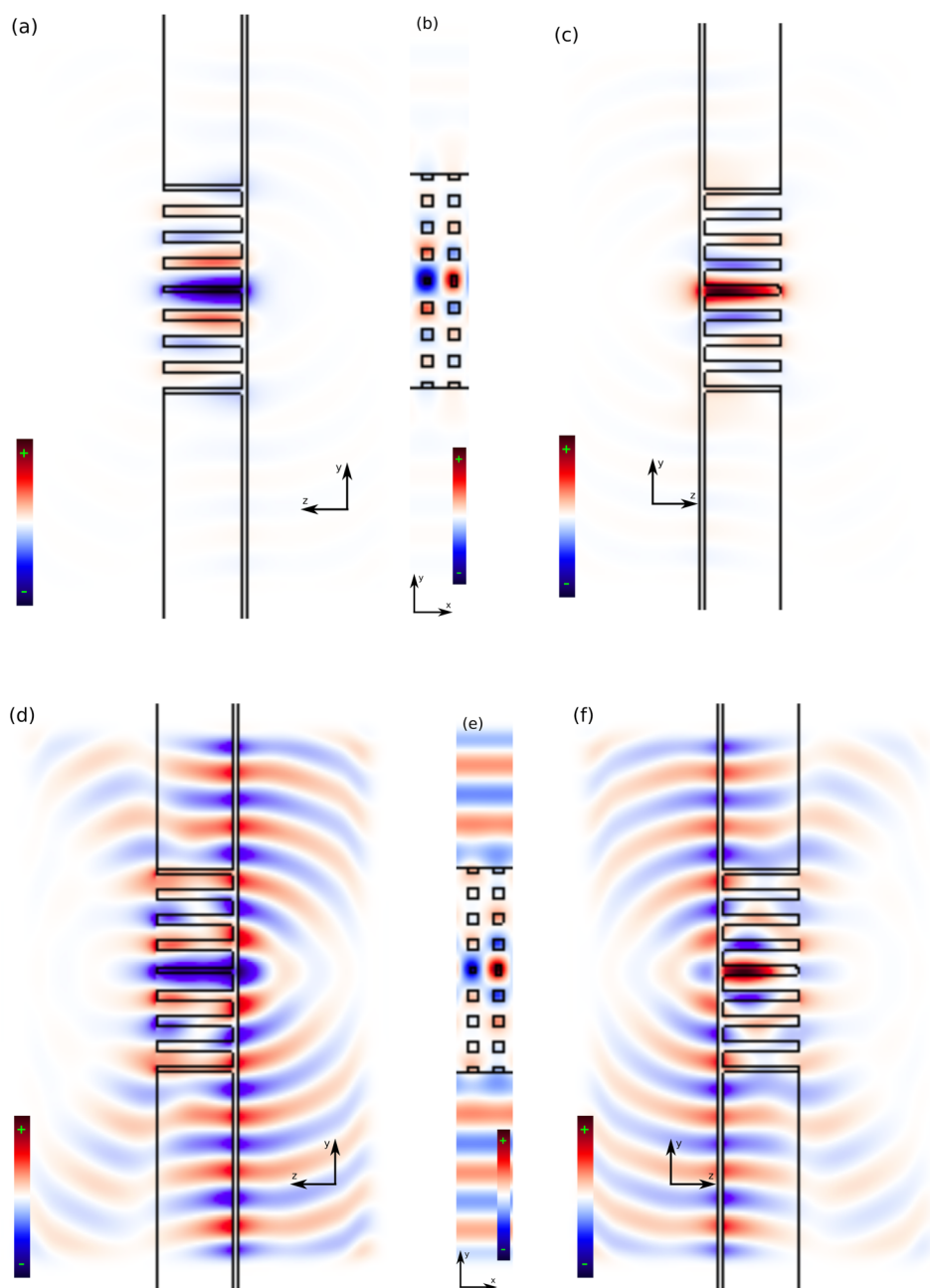


**FIG. 5.** WLM electric field  $[\text{Re}(E_z)]$  snapshots for backed, short-pillar LiPC. Two distinct constituents are observed with strong field localization about the waveguide [(a)–(c)] and weak [(d)–(f)]: (a) profile (yz-slice) of first constituent along centerline of left unit-cell of x-period-doubling, (b) overview (xy-slice) of first constituent at plane through nanopillar z-centers, (c) profile (yz-slice) of first constituent along centerline of right unit-cell of x-period-doubling, (d) profile (yz-slice) of second constituent along centerline of left unit-cell of x-period-doubling, (e) overview (xy-slice) of second constituent at plane through nanopillar z-centers, and (f) profile (yz-slice) of second constituent along centerline of right unit-cell of x-period-doubling.

Three different transmission peaks appear in Figs. 8–14, corresponding to IGBM1, SLMs, and WLM, in order of increasing frequency. Depending on analyte-binding, IGBM1 peaks may redshift and/or undergo transmission-level enhancement. Similarly, WLM may redshift and/or undergo changes to transmission level (both enhancement and suppression). Lastly, the SLM peaks may redshift, change transmission levels, and/or split into two separate peaks.

The IGBM1 fields have a greater overlap with the surface gratings than with the central waveguide. Accordingly, analyte-binding

at  $W$  alone (Fig. 8) does not result in any significant IGBM1 redshift. However, in the cases where either  $N$  or  $F$  or both are involved (Figs. 9–12), the IGBM1 redshift is more perceptible. For these cases, the redshift of the nearby SLM peaks far outpace the IGBM1 redshift. The SLM becomes progressively closer in frequency to the IGBM1, allowing photons at the IGBM1 frequency to pass through the SLM as an off-resonant “virtual state,”<sup>5</sup> resulting in an IGBM1 transmission enhancement. In the case where analyte attaches to both  $N$  and  $F$  (Figs. 13 and 14), the redshift and

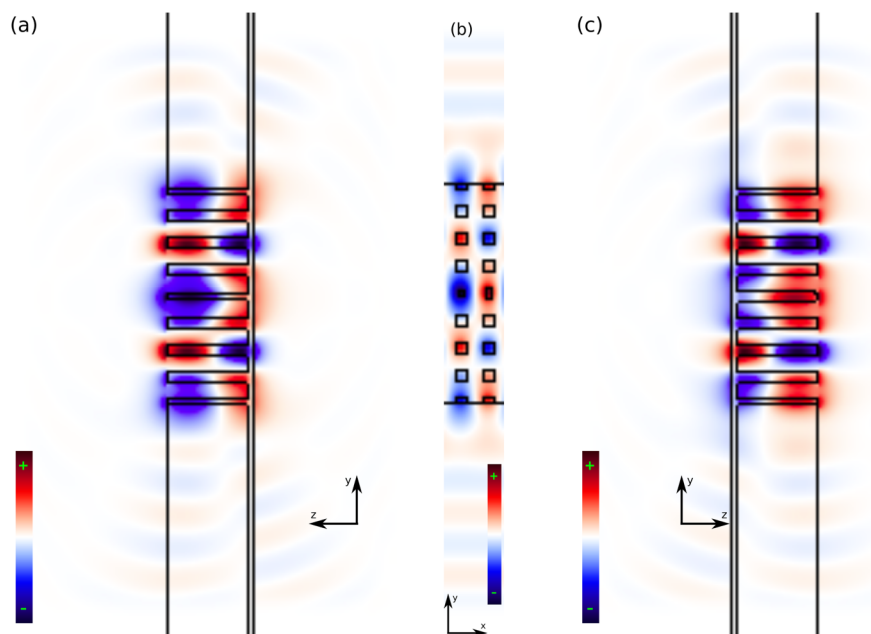


**FIG. 6.** IGBM1 electric field  $[\Re(E_z)]$  snapshots for backed, short-pillar LiPC. Based on number of nodes seen along the  $y$ -direction, this is a lower-order IGBM than the one in Fig. 7 (number of nodes along the  $z$ -direction are the same for both IGBM1 and IGBM2): (a) profile ( $yz$ -slice) along centerline of left unit-cell of  $x$ -period-doubling, (b) overview ( $xy$ -slice) at plane through nanopillar  $z$ -centers, and (c) profile ( $yz$ -slice) along centerline of right unit-cell of  $x$ -period-doubling.

transmission enhancement of IGBM1 is even more significant. The presence of IGBMs in the PBG is a feature specific to our LiPC and does not occur for a pure 2D system.<sup>5</sup>

The WLM redshifts only in the cases where analyte binds to the  $W$  site. This is seen for Figs. 8, 10, 12, and 14. The redshift brings the WLM closer in frequency to the SLM, facilitating tunneling of additional photons at the WLM frequency through the

off-resonant SLM “virtual state,” resulting in WLM transmission enhancement. Corresponding SLM transmission enhancements are only seen when there is no SLM peak-splitting (Figs. 8 and 14), i.e., when analyte binds to both surface gratings of the LiPC. WLM transmission enhancement is a novel feature of the LiPC. In the 2D progenitor of the LiPC,<sup>5</sup> the WLM transmission peaks are already near unity. In other words, almost all source photons emitted at

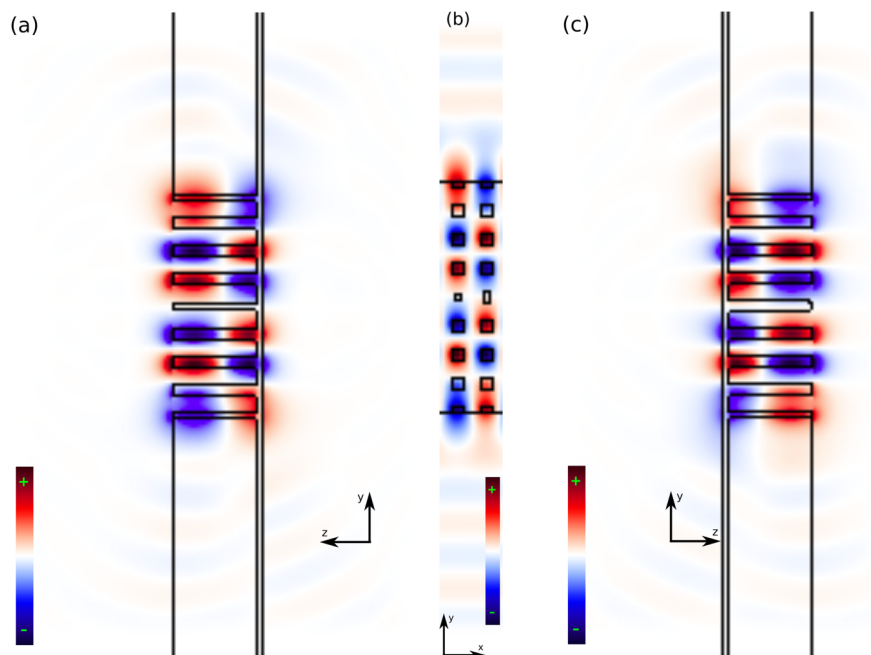


**FIG. 7.** IGBM2 electric field  $[\Re(E_z)]$  snapshots for backed, short-pillar LiPC. Based on number of nodes seen along the  $y$ -direction, this is a higher-order IGBM than the one in Fig. 6 (number of nodes along the  $z$ -direction are the same for both IGBM1 and IGBM2): (a) profile ( $yz$ -slice) along centerline of left unit-cell of  $x$ -period-doubling, (b) overview ( $xy$ -slice) at plane through nanopillar  $z$ -centers, and (c) profile ( $yz$ -slice) along centerline of right unit-cell of  $x$ -period-doubling.

TABLE I. Summary of acronyms used.

Acronym	Expansion	Definition and/or remarks
PC	Photonic crystal	An artificial dielectric material with periodic variations at the scale of roughly half the wavelength of light that may facilitate a photonic bandgap
PBG	Photonic bandgap	A band of optical frequencies at which light propagation within a PC (cf. definition above) is forbidden in all directions
PCF	Photonic crystal fiber	A waveguide with a cross section that incorporates a point-defect at the center of a two-dimensional PC, often allowing a lower-index core (i.e., the defect) to be clad in a higher-index dielectric material (i.e., the PC) in contrast to traditional index-guiding
LiPC	Lab-in-a-photonic-crystal	A sensing device contained within a PC architecture that leverages optical sensing modes engineered within the PBG associated with the structure (cf. Fig. 1 for the design presented in this discussion)
$N$	Near-to-source surface grating	Alternatively referred to as the proximal surface grating from the optical source (cf. Fig. 1)
$W$	Waveguide grating	Located between $N$ and $F$ gratings (cf. Fig. 1)
$F$	Far-from-source surface grating	Alternatively referred to as the distal surface grating from the optical source (cf. Fig. 1)
SLM	Surfacelike mode	A hybridized sensing mode of the device in Fig. 1 predominantly due to field localization at the surface gratings $N$ and $F$ , and possibly, with field contributions from the waveguide region $W$ (cf. Fig. 4)
WLM	Waveguidelike mode	A hybridized sensing mode of the device in Fig. 1 predominantly due to field localization at the waveguide $W$ , with field contributions from the surface grating regions $N$ and $F$ (cf. Fig. 5)
IGBM	Index-guided bulk mode	A mode introduced into the intrinsic (i.e., defect-free) region of the 2D-PC due to finite extension into the $z$ -direction: Fields are trapped within the PC region, which features a PBG in the $x$ - and $y$ -directions, due to index-guiding along the $z$ -direction (cf. Figs. 6 and 7).

the WLM resonance pass through the 2D system without the aid of nearby, off-resonant virtual states. However, due to diffraction losses in the third dimension, not all the photons emitted by the source at the WLM resonance frequency transit through the LiPC along the light propagation direction. Under favorable circumstances, more photons can be diverted from diffractive losses into the WLM transmission channel. On the other hand, small suppressions to the WLM transmittance are observed when analyte-binding occurs at  $N$  and/or  $F$ , but not at  $W$ . In these cases, the SLM peak(s) move away from the WLM frequency, resulting in weaker virtual-state-coupling, as shown in Figs. 9, 11, and 13.

SLM behavior is among the unique features of our LiPC design, enabling it to supersede the performance of its 2D progenitor. For the case of analyte-binding to only one of  $N$  or  $F$  (Figs. 9–12), the SLM peak is seen to split into two, as the near-degenerate, weakly coupled surface grating modes move significantly far apart in frequency. One limitation of the pure 2D prototype<sup>5</sup> is its inability to distinguish between analyte-binding at  $N$  vs  $F$ . This is remedied in the LiPC by the higher intensity of light at  $N$  compared to the depleted intensity at  $F$  due to scattering of source light into the third dimension. In the cases where analyte binds to the surface grating  $F$  which lies distal from the light source, SLM peak-splitting is due to a redshift of the surface mode at  $F$ . The redshifted peak is noticeably transmission-suppressed as a significant number of photons leak out of the LiPC prior to reaching this exit-surface. In the case of analyte-binding to  $N$ , which lies proximal to the light source, the SLM peak-splitting occurs due to a redshift of the surface mode at  $N$ , which has a

higher concentration of photons before they have had a chance to leak from the LiPC. This leads to an enhanced transmission of the shifted peak, which can also make use of the IGBM1 virtual states as a result of their proximity in frequency space. The suppressed  $F$  peaks in the SLM split in Figs. 11 and 12 are discernible from the enhanced  $N$  peaks in Figs. 9 and 10, resulting in a way of distinguishing analyte-binding at  $F$  vs  $N$ . When analyte binds to both surface gratings  $N$  and  $F$ , there is no SLM peak-splitting (Figs. 13 and 14). Rather, a redshift occurs, bringing the entire SLM closer in frequency to the nearby IGBM1 and resulting in enhanced photon-tunneling and SLM transmission enhancement, with a corresponding enhancement to IGBM1.

In Appendix E, we quantify the foregoing discussion on LiPC sensor performance, tracking the peak frequencies, maximal transmittances, and Q-factors for various analyte combinations and thicknesses. We collate qualitative behavior of the LiPC transmittance into Table II for three analytes  $\alpha$ ,  $\beta$ , and  $\gamma$ , which bind to sites  $F$ ,  $N$ , and  $W$ , respectively. For our LiPC, all eight possible analyte-binding configurations are distinguishable, compared to only six in a pure 2D system.<sup>5</sup> For peak shifts, enhancements, and suppressions in Table II, lengths of the respective arrows are representative of the extent of the behavior observed.

In summary, we have demonstrated the operation of a LiPC capable of differentiating between all eight possible configurations of analyte-binding at three different sites. Discrimination of analyte-binding at the two surface gratings  $N$  and  $F$  is made possible by the progressive diffraction of light into the third dimension

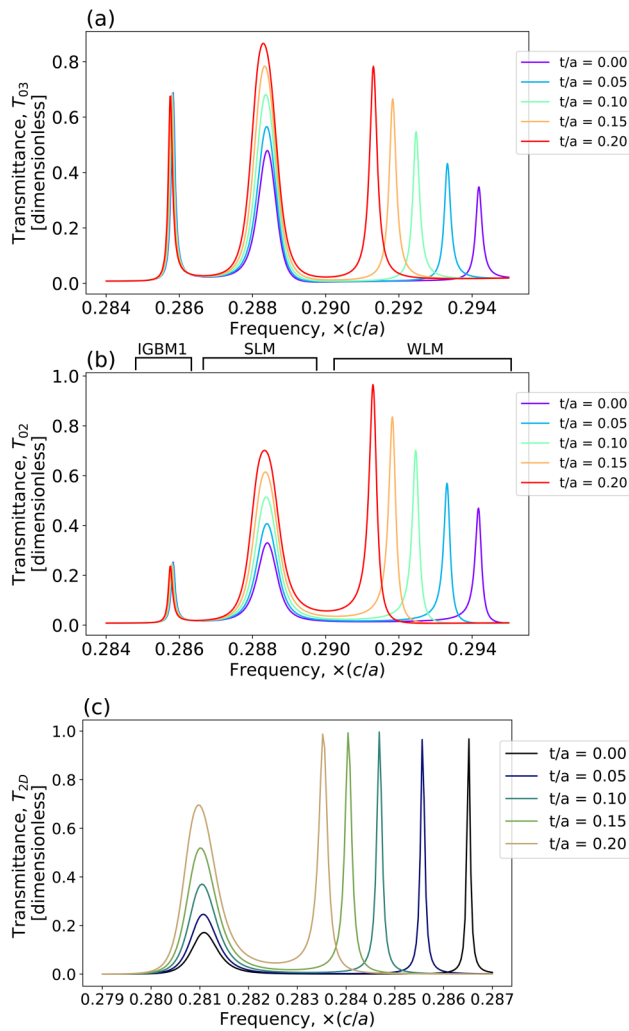


**FIG. 8.** Spectral results for W-binding in the backed, short-pillar LiPC. (a) and (b) Transmittances at detector locations O2 and O3; positions of thin-silver detectors are as seen in Fig. 3. Sliver detector O3 in (a) is deemed the best for sensing, while detector O2 in (b) best replicates the 2D prototype's results. Approximate frequency ranges of IGBM1, SLM, and WLM peaks are shown in (b). (c) Results from the 2D prototype for comparison: maximum WLM transmittance for the 2D prototype is already saturated and cannot be amplified further.

as it propagates farther through the LiPC. This scattering of light into the  $z$ -direction also leads to discernible transmission-level changes as the interaction between resonance modes changes with specific analyte-bindings. In terms of concrete physical dimensions, for an illuminating wavelength  $\lambda_0 = 1.5 \mu\text{m}$  and a center frequency  $a/\lambda_0 \approx 0.290$  (cf. center of spectral windows presented in Figs. 8–14), our structure has a PC unit-cell length of  $a \approx 435 \text{ nm}$  and requires fabrication precision of  $0.1 \times a \approx 45 \text{ nm}$  (corresponding to FDTD spatial resolution of 10 mesh points per PC unit-cell side-length  $a$ ). Based on FDTD results presented

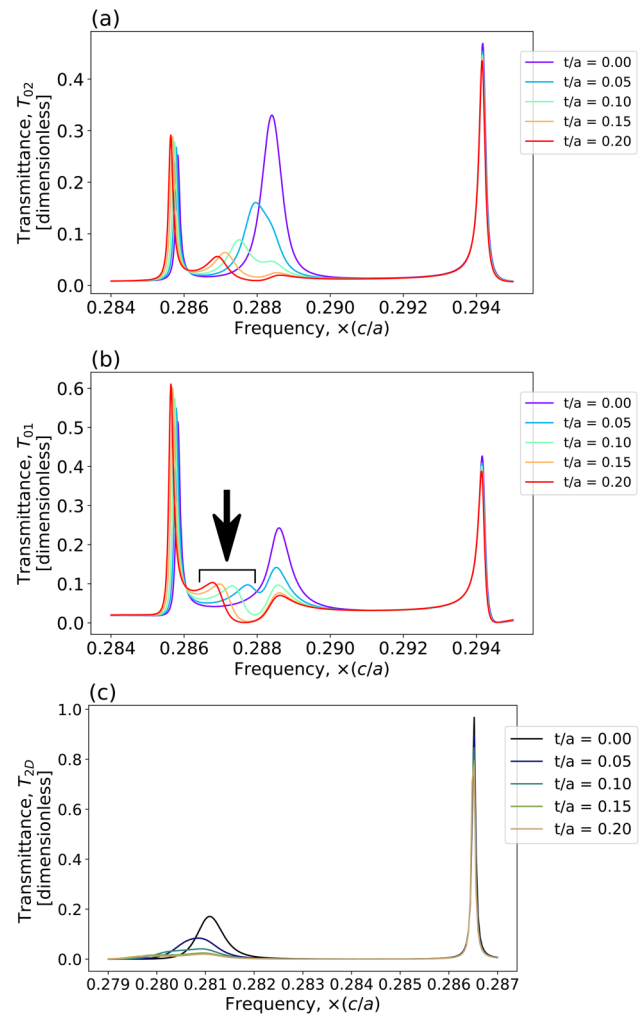


**FIG. 9.** Spectral results for N-binding in the backed, short-pillar LiPC. (a) and (b) Transmittances at detector locations O2 and O1; positions of thin-silver detectors are as seen in Fig. 3. Sliver detector O1 in (b) is deemed the best for sensing, while detector O2 in (a) best replicates the 2D prototype's results. Results in (b) are distinguishable from Fig. 11(b) by the presence of a pronounced low-frequency SLM split peak (indicated by an arrow). (c) Results from the 2D prototype for comparison: results are indistinguishable from those in Fig. 11(c).

above (cf. Figs. 8–14), an upper bound to the limit-of-detection of analyte layers is  $\Delta t^{(min;FDTD)} = 0.05 \times a \approx 25 \text{ nm}$ . If using  $\lambda_0 = 5 \mu\text{m}$  instead, a fabrication precision of  $0.1 \times a \approx 150 \text{ nm}$  yields an upper-bound estimate of  $\Delta t^{(min;FDTD)} = 0.05 \times a \approx 75 \text{ nm}$  to the limit-of-detection for analyte layers.

#### IV. FLUID REFRACTIVE-INDEX CALIBRATION

As described above, our LiPC exhibits transmission peaks due to index-guided bulk modes (IGBMs) not present in 2D. These

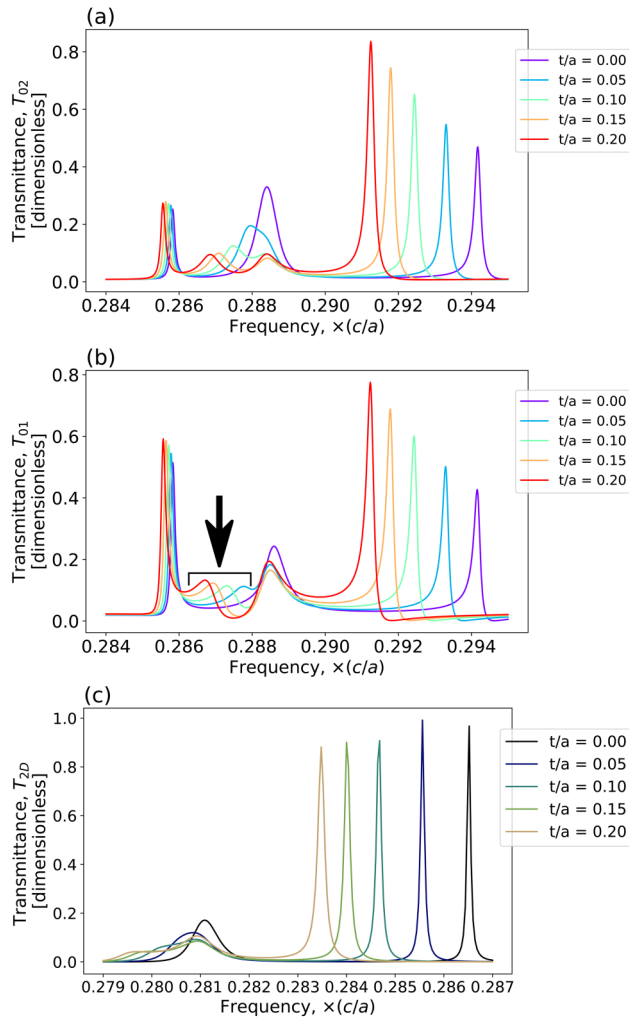


**FIG. 10.** Spectral results for WN-binding in the backed, short-pillar LiPC. (a) and (b) Transmittances at detector locations 02 and 01: positions of thin-silver detectors are as seen in Fig. 3. Sliver detector 01 in (b) is deemed the best for sensing, while detector 02 in (a) best replicates the 2D prototype's results. Results in (b) are distinguishable from those in Fig. 12(b) by the presence of a pronounced low-frequency SLM split peak (indicated by an arrow). (c) Results from the 2D prototype for comparison: WLM peak transmittance amplification does not occur due to increasing WLM-SLM separation as a result of SLM peak-split. Results are indistinguishable from those in Fig. 12(c).

IGBMs are vertically localized within the overall higher-index LiPC active region sandwiched between lower-index fluid above and glass below. As seen in Fig. 6, IGBM1 optical fields are distributed diffusely over the computational domain, with significant penetration into the high-index nanopillars as well as the infiltrating liquid material. It is possible that the average fluid refractive index,  $n_{bg}$ , may fluctuate due to undesirable impurities irrelevant to the primary sensing task. Here, we discuss the use of IGBM1 and SLM peak positions to detect fluctuations in  $n_{bg}$  for sensor calibration.

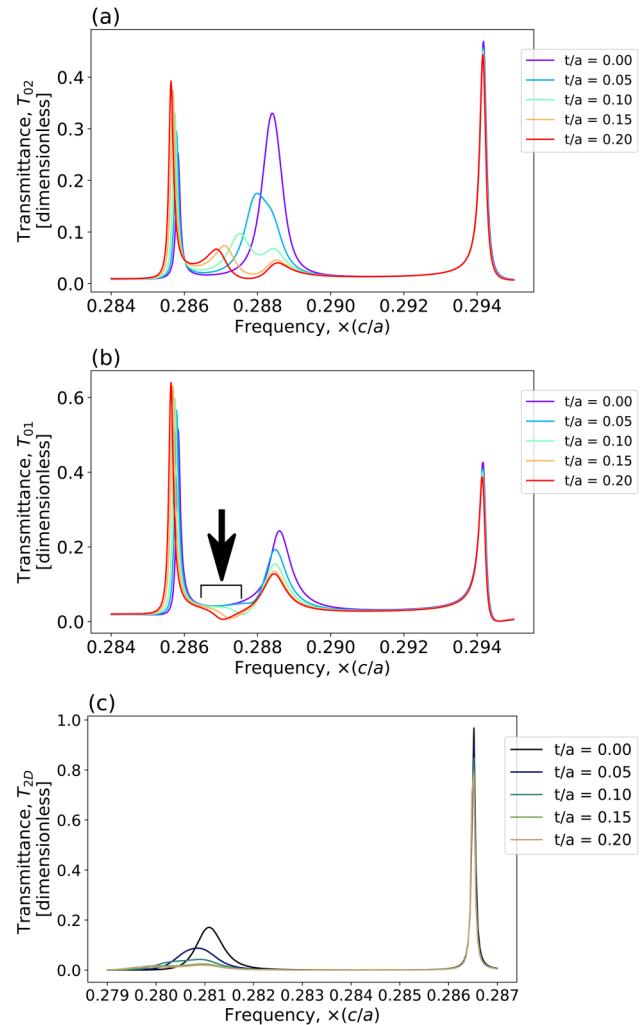


**FIG. 11.** Spectral results for F-binding in the backed, short-pillar LiPC. (a) and (b) Transmittances at detector locations 02 and 01: positions of thin-silver detectors are as seen in Fig. 3. Sliver detector 01 in (b) is deemed the best for sensing, while detector 02 in (a) best replicates the 2D prototype's results. Results in (b) are distinguishable from those in Fig. 9(b) by a suppressed low-frequency SLM split peak (indicated by an arrow). (c) Results from the 2D prototype for comparison: results are indistinguishable from those in Fig. 9(c).

In Fig. 15, we consider the  $t/a = 0.0$  case for  $n_{bg} \in \{1.300, 1.325, 1.350, 1.375, 1.400\}$  with a view to detecting fluctuations of  $n_{bg}$  around the design parameter  $n_{bg} = 1.35$ . For simplicity, we only focus on the transmittance in the thin-silver detector labeled 04, which lies near the LiPC-fluid interface at the top of the device in Fig. 3. We identify in Fig. 15 the IGBM1 and SLM peaks corresponding to the various  $n_{bg}$  values in consideration. The peak frequencies for both IGBM1 and SLM display monotonic redshifts in response to  $n_{bg}$  increments, as expected. The SLM redshifts occur at a markedly slower rate than the IGBM1 shifts, allowing the IGBM1 peaks to catch up to the SLM peaks at the lowest  $n_{bg}$ .

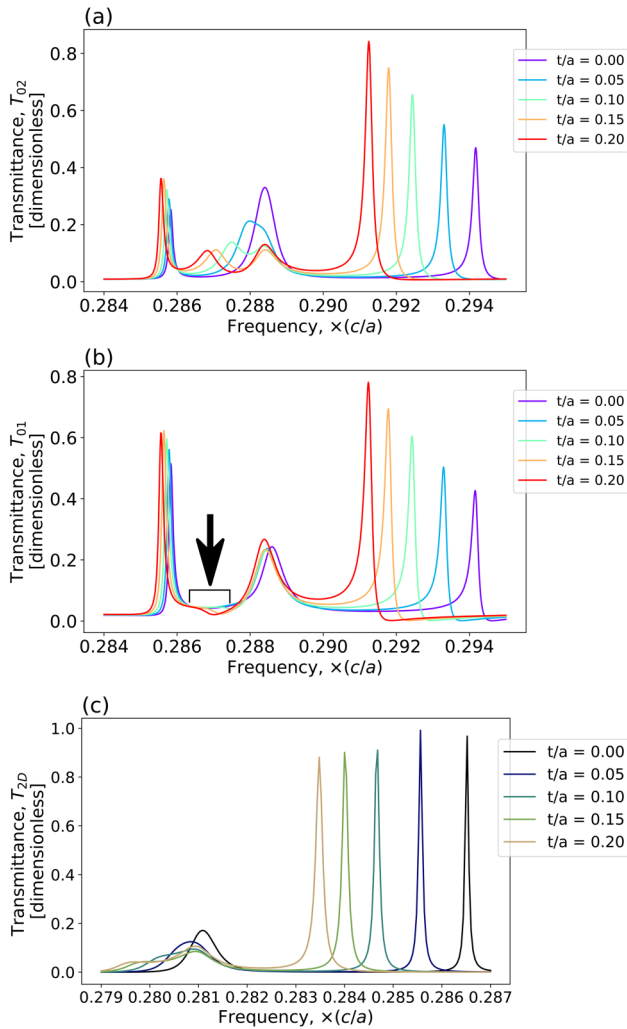


**FIG. 12.** Spectral results for WF-binding in the backed, short-pillar LiPC. (a) and (b) Transmittances at detector locations O2 and O1: positions of thin-sliver detectors are as seen in Fig. 3. Sliver detector O1 in (b) is deemed the best for sensing, while detector O2 in (a) best replicates the 2D prototype's results. Results in (b) are distinguishable from those in Fig. 10(b) by a suppressed low-frequency SLM split peak (indicated by an arrow). (c) Results from the 2D prototype for comparison: WLM peak transmittance amplification does not occur due to increasing WLM-SLM separation as a result of SLM peak-split. Results are indistinguishable from those in Fig. 10(c).

The IGBM1 peak transmittances also increase monotonically with  $n_{bg}$  decrements due to off-resonant tunneling through the SLM at IGBM1 frequencies. For  $n_{bg} = 1.300$ , the IGBM1 and SLM are almost coincident in frequency, resulting in a very broad transmission peak.

The monotonic,  $n_{bg}$ -induced redshifts for IGBM1 and SLM modes are seen in Fig. 16(a). Figure 16(b) summarizes the corresponding peak transmittance behavior. This suggests that the positions and peak transmittance-levels for the IGBM1 and SLM

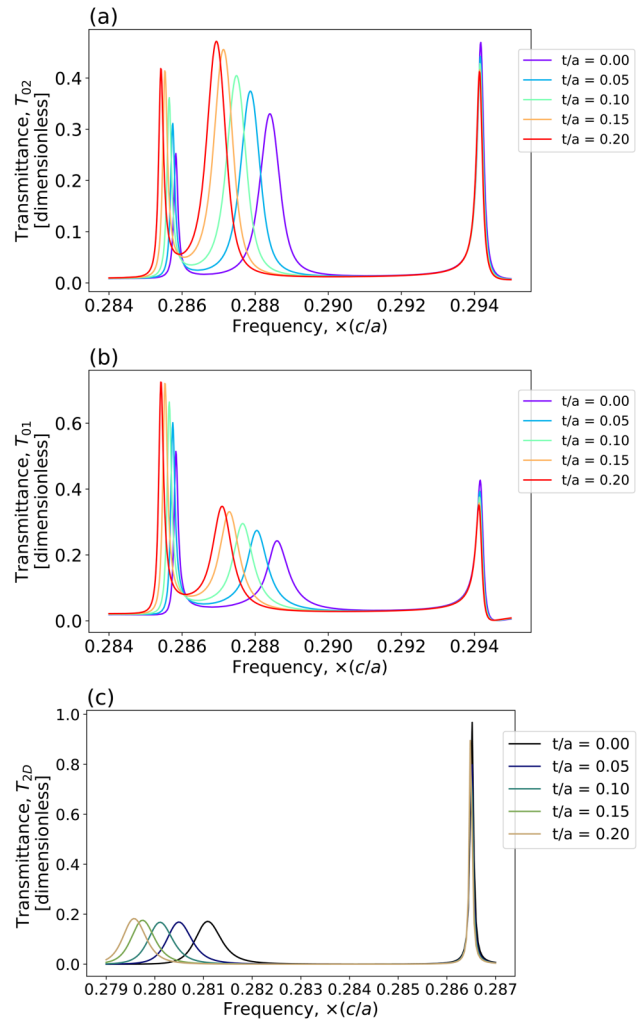


**FIG. 13.** Spectral results for NF-binding in the backed, short-pillar LiPC. (a) and (b) Transmittances at detector locations O2 and O1: positions of thin-sliver detectors are as seen in Fig. 3. Sliver detector O2 in (a) is deemed the best for sensing, while detector O1 in (b) best replicates the 2D prototype's results. (c) Results from the 2D prototype for comparison: the absence of an IGBM near the SLM in the 2D prototype causes its maximum SLM transmittances to be smaller compared to WLM transmittances.

resonances at detector 04 may be used to calibrate the LiPC under conditions of variable  $n_{bg}$ .

## V. ROBUSTNESS OF SENSOR CHARACTERISTICS TO FABRICATION DEFORMITIES

We now examine the fidelity of our LiPC despite structural imperfections and distortions in the nanopillar array. For concreteness, we focus on the WN analyte-binding case for  $t/a \in \{0.00, 0.10\}$ . The SLM, WLM, IGBM1, and IGBM2 peaks for nanopillars with a constant square cross section are identified in

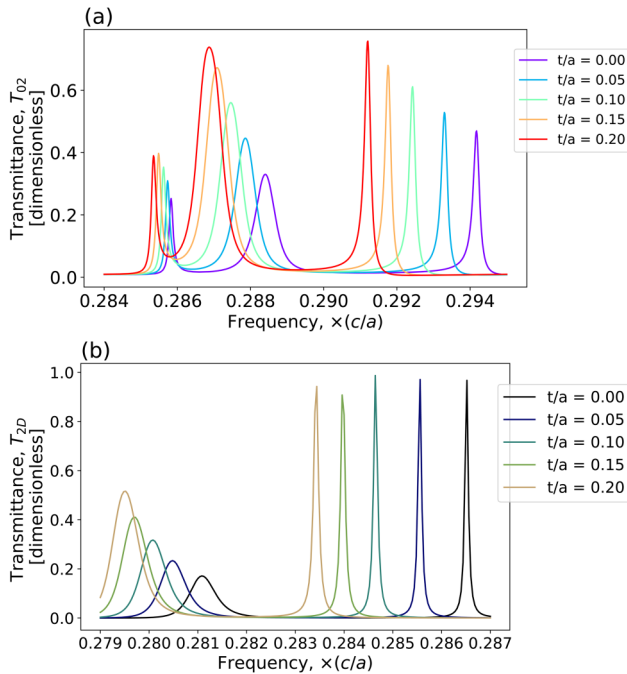


**FIG. 14.** Spectral results for WNF-binding in the backed, short-pillar LiPC. (a) Transmittance at detector location O2: positions of thin-silver detectors are as seen in Fig. 3. Both the best sliver detector for sensing and the best replication of the 2D prototype's results occur at detector labeled O2. Unsaturated WLM transmittances undergo enhancement as more photons can be harvested from the illuminating source and channeled through the WLM. (b) Results from the 2D prototype for comparison: the absence of an IGBM near the SLM in the 2D prototype causes its maximum SLM transmittances to be smaller compared to WLM transmittances.

Fig. 17(a) for ready comparison with deformed structures. We refer to undeformed nanopillars as having a *flare factor* of unity. We limit our discussion to results from a single representative thin-silver detector for each of the deformation types considered for brevity.

We first consider *WN* analyte-binding with  $t/a \in \{0.00, 0.10\}$  for an isoareal deformation of the square cross section of each nanopillar into a circle. The circles have a radius of

$r = \pi^{-1/2} \times w$ , where  $w = 0.4 \times a$  is the side-length of the original 2D PC square. Analogous changes are made to the waveguide and surface grating regions. Transmission spectra for this deformation are plotted in Fig. 17(b), illustrating SLM, WLM, IGBM1, and IGBM2 peak behaviors as seen by a detector placed at a level of  $\frac{1}{2} \times d$  above the backing layer. Comparing circular nanopillar spectra with those for square ones in Fig. 17(a), we observe good agreement. The SLM peak shifts, splits, and attenuates in intensity as in the square cross-section case. The WLM peak shifts and amplifies in intensity. The IGBM1 and IGBM2 peaks for the circular cross-section case behave consistently, but IGBM2 appears more sensitive to analyte-binding than in the square cross-section case. Furthermore, modes of the circular cross-section nanopillar LiPC have lower Q factors than those for square cross section. As a result, the modes for circular nanopillars span a wider set of frequencies and interact more strongly with each other. Accordingly, intermodal coupling effects, such as SLM peak-splitting, are more readily observed. Based on the foregoing, we expect the LiPC design to be fairly robust to rounded corners of the nanopillars.

Next, we consider nanopillars of cross section that narrows with height. Nanopillars formed by certain experimental techniques<sup>30,31</sup> tend to be thicker at the base than at the top. We consider deformed nanopillars to be *pyramidal frusta* isovolumetric to the original uniform square cross-section case. We expand the base to have side-length  $w_{bottom} = 1.2 \times w$  and, correspondingly, narrow the top cross section to have side-length  $w_{top} = (-0.6 + \sqrt{1.92}) \times w$ . These modifications are also made for nanopillars constituting the surface and waveguide regions. We refer to these deformed nanopillars as having a flare factor of 1.2. Transmission spectra are shown in Fig. 17(c) for detector O4 near the top of the LiPC. The SLM, WLM, IGBM1, and IGBM2 behaviors are qualitatively similar to the uniform square nanopillar case in Fig. 17(a). However, the sensor performance degrades slightly. First, the WLM peak-shift is less pronounced, resulting in worse sensitivity to analyte thickness. Second, the SLM peak-splitting behavior is noticeably absent, although a peak-shift is still observed. Third, both IGBM1 and IGBM2 peaks are less sensitive to analyte-binding. For the case of IGBM1, this could have implications for  $n_{bg}$  calibration, as described above. In spite of these deviations from ideality, our sensor is still able to provide essential data on analyte-binding for a flare factor of 1.2. In other words, the LiPC retains its sensing capabilities under moderate distortion of the nanopillar shape.

**TABLE II.** Transmission spectrum response of the LiPC to increase of analyte-layer thickness for all possible analyte-binding configurations. All eight possible analyte-binding configurations are distinguishable in the LiPC. Detector labels are explained in Fig. 3.

$\alpha$	$\beta$	$\gamma$	Figure	Detector label	$\omega_{IGBM1}$	$T_{peak, IGBM1}$	$\omega_{SLM}$	$T_{peak, SLM}$	$\omega_{SLM}$ split?	$\omega_{WLM}$	$T_{peak, WLM}$
0	0	0	N/A	N/A		—			N	—	
0	0	1	8	03	←	—		↑	N	←	↑
0	1	0	9	01	←	↑	←	↓ colon ↓	Y		↓
0	1	1	10	01	←	↑	←	↓ colon ↓	Y	←	↑
1	0	0	11	01	←	↑	←	↓ colon ↓	Y		↓
1	0	1	12	01	←	↑	←	↓ colon ↓	Y	←	↑
1	1	0	13	02	←	↑	←	↑	N		↓
1	1	1	14	02	←	↑	←	↑	N	←	↑

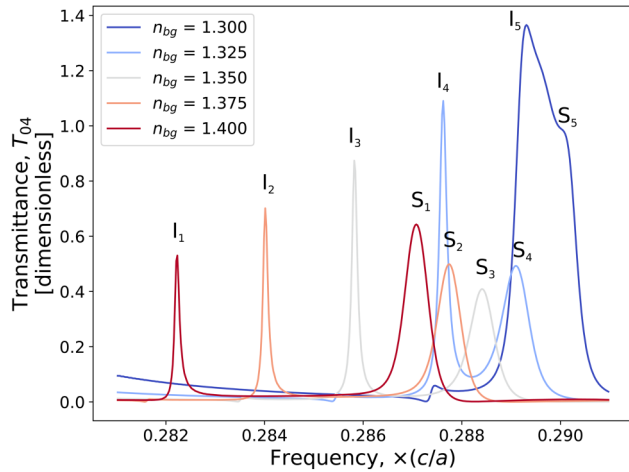


**FIG. 15.** Transmittance variations at detector 04 for fluid background index changes in the backed, short-pillar LiPC. IGBM1 peaks are identified in order of increasing frequency as  $I_1$  (for  $n_{bg} = 1.400$ ),  $I_2$  (for  $n_{bg} = 1.375$ ),  $I_3$  (for  $n_{bg} = 1.350$ ),  $I_4$  (for  $n_{bg} = 1.325$ ), and  $I_5$  (for  $n_{bg} = 1.300$ ). SLM peaks are identified in order of increasing frequency as  $S_1$  (for  $n_{bg} = 1.400$ ),  $S_2$  (for  $n_{bg} = 1.375$ ),  $S_3$  (for  $n_{bg} = 1.350$ ),  $S_4$  (for  $n_{bg} = 1.325$ ), and  $S_5$  (for  $n_{bg} = 1.300$ ). The peaks redshift with increasing  $n_{bg}$ , while changes in their level of mutual interaction lead to transmission-level variations. The normal case of  $n_{bg} = 1.350$  is represented by  $I_3$  and  $S_3$ . Peaks  $I_5$  and  $S_5$  are very close in frequency, giving rise to a very broad peak with very high transmittance.

Finally, we consider the extreme case where the nanopillars are deformed into full-fledged pyramids isovolumic to the original nanopillars. Here, for regular nanopillars,  $w_{bottom} = w \times \sqrt{3}$  and  $w_{top} = 0$  (and similarly for the surface and central-waveguide nanopillars), amounting to a flare factor of  $\sqrt{3}$ . Figure 17(d) shows that the device has now effectively lost its sensing capabilities. The higher fraction of low-index liquid near the top of the LiPC causes the lower edge of the 2D PBG to blueshift, encroaching into the original free spectral range. The upper edge of the 2D PBG also appears to have become malformed.

We comment briefly on *random fabrication defects* that degrade PCs in general. Small random fluctuations are already accounted for by the low resolution (10 mesh points per 2D-PC unit-cell period  $a$ ) of our FDTD calculations. Moreover, we undertake  $\epsilon$ -averaging over a submesh (10 submesh points per mesh point), resulting in pseudorandom fluctuations of  $\epsilon$  at interfaces of different materials. This accommodates random disorder on the scale of  $0.1 \times a$ , suggesting our results are robust to random structural variations on this scale.

In summary, our LiPC exhibits robustness of sensing characteristics under (a) random structural disorder of the scale of  $0.1 \times a$ , (b) systematic fabrication issues that round the corners of the square cross-section nanopillars, and (c) thickening of about 20% at the nanopillar bases.

## VI. DISCUSSION AND CONCLUSION

We have presented a precise and comprehensive design of an optical biosensor operating on a fundamentally different principle

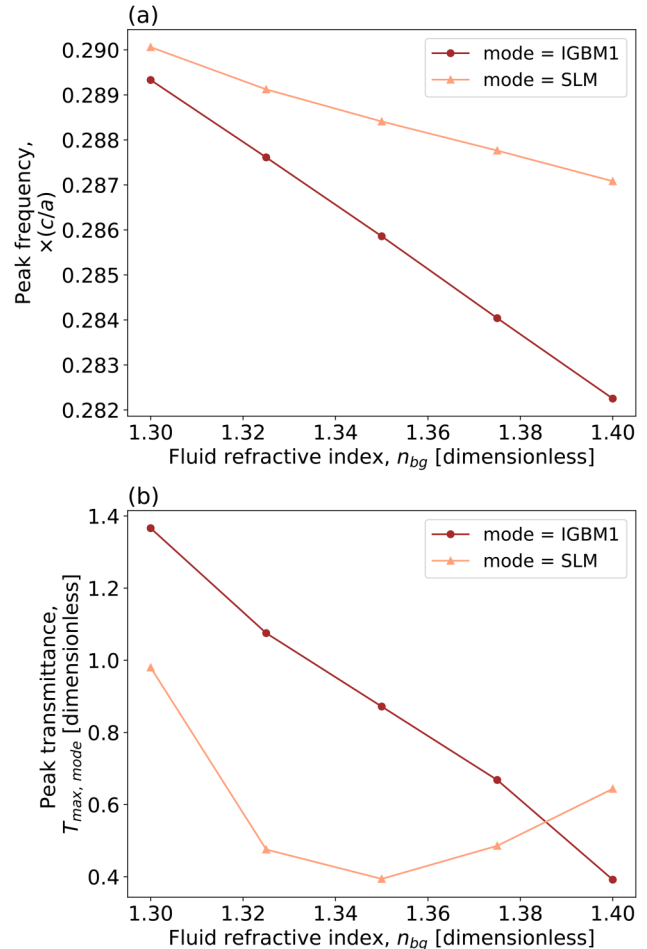


**FIG. 16.** Calibration curves for background fluid refractive index in the backed, short-pillar LiPC. (a) Frequency Variation and (b) peak transmittance variation for IGBM1 and SLM: the values shown here can be used to calibrate the LiPC device under conditions of variable fluid refractive index.

than single cavity-mode sensors. The operating principle of our sensor combines the conventional refractive-index-induced frequency-shift of individual optical resonances with the analyte-binding-induced shift in coupling between nearby resonances. If the individual resonance frequencies are considered as diagonal elements of a matrix and the coupling between resonance modes are considered off-diagonal elements of the same matrix, then disease-marker bindings in our biosensor result in shifts of both the diagonal *and* off-diagonal elements. Almost all previous biosensors capable of detecting multiple disease-markers operate on only the shift of diagonal elements, with the off-diagonal elements typically zero. Our operating principle produces a complex spectral fingerprint for each combination of disease-markers (analytes) present in a given sample. This fingerprint consists of conventional peak-shifts supplemented by transmission-level changes and peak-splitting and can logically discriminate between different types of analytes and various

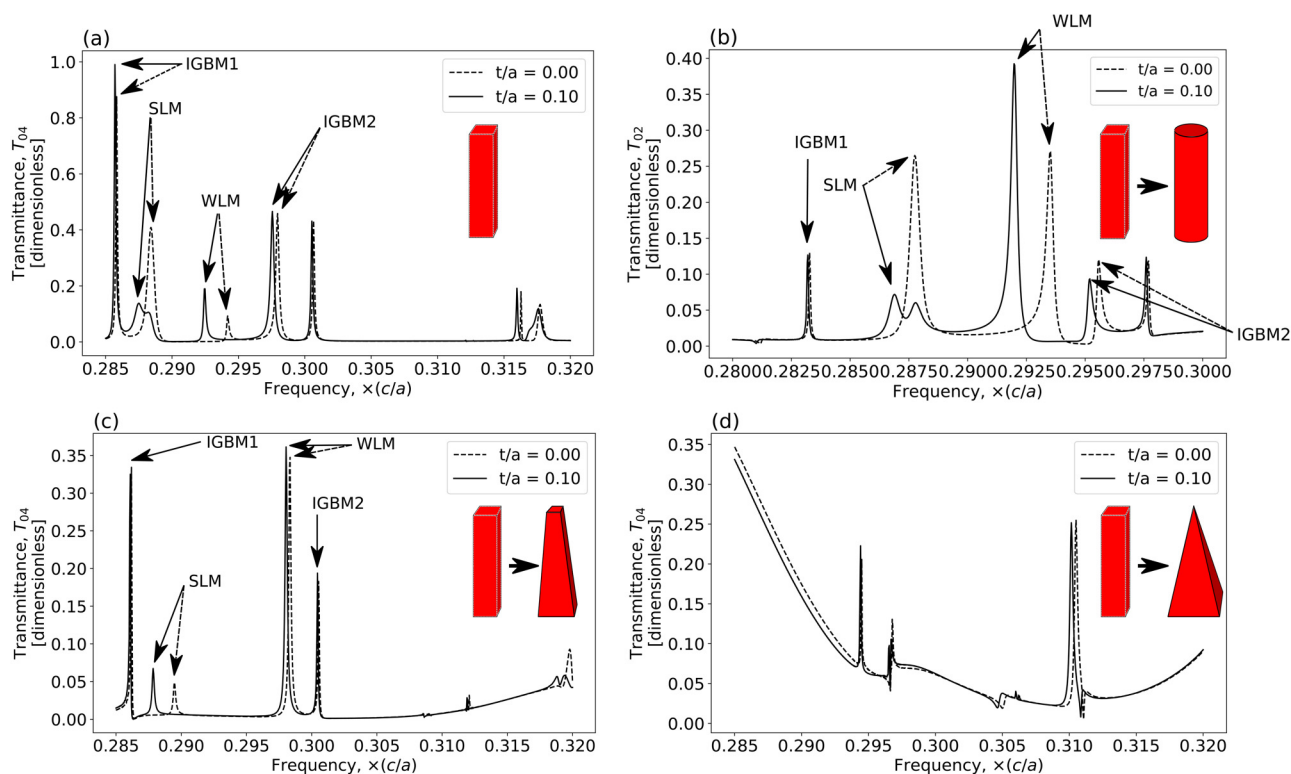


**FIG. 17.** Comparison of spectral signatures of various structural deformations of the backed, short-pillar LiPC using the WN analyte-binding case. (a) Undeformed reference case of uniform square cross-section nanopillars: transmission peaks for SLM, WLM, IGBM1, and IGBM2 are identified for detector 04. (b) Isoareal deformation of uniform nanopillar cross sections from squares to circles: transmission peaks for SLM, WLM, IGBM1, and IGBM2 are identified for detector 02. Modes have lower Q-factors and exhibit stronger collaborative effects than in (a). Sensing abilities are well-retained for rounding of nanopillar corners. (c) Isovolemic deformation of uniform square cross-section nanopillars to pyramidal frusta with 20% side-length expansion at base: transmission peaks for SLM, WLM, IGBM1, and IGBM2 are identified for detector 04. Some essential sensing properties, such as peak-shifting is retained in this case, but other sensing features are lost. (d) Isovolemic deformation of uniform square cross-section nanopillars to full-fledged pyramids: results from detector 04 indicates a malformed 2D PBG, as well as compromised sensing capabilities.

concentrations thereof. In other words, a single optical measurement, using very small sample volume, can provide diagnostic information about complex diseases, as well as different stages of a given disease. Since all optical modes in our system are extended waveguide modes, the binding of disease-markers is more certain in a shorter time interval, facilitating nearly-instantaneous detection.

Our fabrication-ready design of a Lab-in-a-Photonic-Crystal (LiPC) optical biosensor consists of nanopillars supported by a thin, high-index backing placed within a glass-trough microfluidic channel. A sensing mechanism based on weak coupling of the photonic bandgap (PBG) surface modes and line-defect waveguide modes was numerically demonstrated. In the present design, we used single-mode waveguides at the center and edges of the PC. Detection of a larger number of disease-markers is also possible through the design of a multimode waveguide within the LiPC.<sup>20</sup> A fabrication scheme for the LiPC device, leveraging standard semiconductor microlithography and emerging technologies, such as high-resolution ink-jet printing, was outlined, and the robustness of our sensing mechanism to fabrication deformities was demonstrated.

For the current implementation of our biosensing mechanism and device design, longer optical wavelengths, say, in the 5–10  $\mu\text{m}$  range, may be advantageous for low-resolution ink-jet functionalization of the LiPC. As the resolution of the functionalization process is improved, the operating wavelength of our sensor may be reduced to, say, 1.5  $\mu\text{m}$  scale. In our current LiPC design, it was shown that the height of the nanopillar array can be reduced by a factor of 2 using a thin silicon ( $n = 3.4$ ) backing layer between the silica substrate ( $n = 1.5$ ) and the silicon pillars. This enabled nanopillars of height  $d = 3 \times a$ , where  $a$  is the lattice constant of the photonic crystal. Further research is needed to determine whether the nanopillar height can be reduced to  $d = 1 \times a$  while maintaining full functionality described in our current design. If this can be achieved, the fabrication of our LiPC may be amenable to low-cost, high-throughput technologies, such as nanoimprinting.

It is hoped that our current design, amenable to fabrication and real-world operation, will stimulate exploration of our distinctive method of Lab-on-Chip biosensing with enhanced capability for disease diagnosis and discrimination.

ACKNOWLEDGMENTS

We are grateful to Professor D. Vujic, Professor O. Levi, and Professor C. Jagadish for helpful discussions and to the Natural Sciences and Engineering Research Council of Canada for financial support.

APPENDIX A: DESIGN CONSIDERATIONS: UNBACKED, LONG NANOPILLAR LAB-IN-A-PHOTONIC-CRYSTAL

Here, we describe the initial design iteration leading to the LiPC presented in Fig. 1 and elucidate the underlying principles. We point out that the behavior of the 2D conceptual prototype for multiplexed biosensing<sup>5</sup> can be recaptured by an infinite extension of the nanopillars along the  $z$ -direction and setting the vertical component of the light propagation wave vector as  $k_z = 0$ . In our LiPC design, we investigate various *finite* nanopillar heights  $d$  and allow optical diffraction and scattering into the third dimension. The initial design for the LiPC is illustrated in Fig. 18. This consists of a glass ( $n = 1.5$ ) base, which extends to  $z \rightarrow -\infty$  for our modeling purposes and acts as a support for the dielectric nanopillars of  $n = 3.4$  as well as the fluid ( $n = 1.35$ ) component. Extending the glass terminations of the 2D paradigm to the same vertical height as the nanopillars creates a natural trough for biomarker flow. The 2D nanopillar array within the trough allows both fluid flow and selective attachment of disease-markers along specific lines of functionalized surfaces. The fluid-flow channel of depth  $d$  has an *open-top*, and the entire structure is considered to be submerged by fluid ( $n = 1.35$ ), which essentially extends to  $z \rightarrow +\infty$  in our

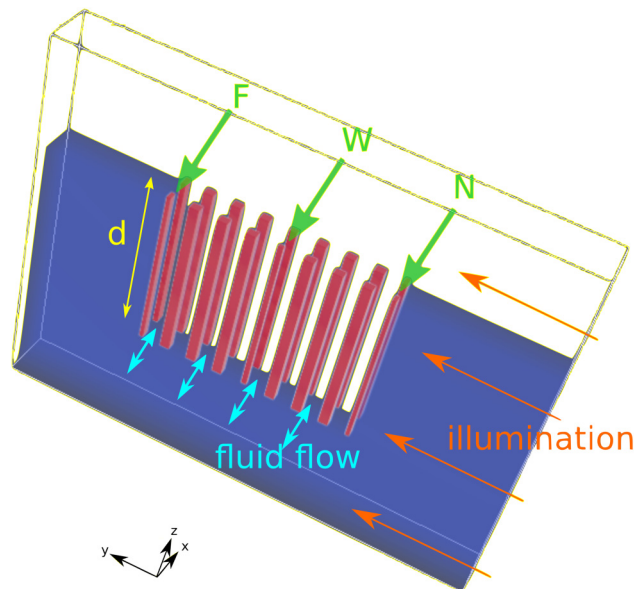


FIG. 18. Design for the LiPC without high-index backing. The structure is a  $z$ -extended version of Fig. 2(b) resting on an infinite glass base and open to fluid from the top. The structure is periodic along the fluid-flow direction. Analyte-binding sites  $N$ ,  $W$ , and  $F$  are identified.

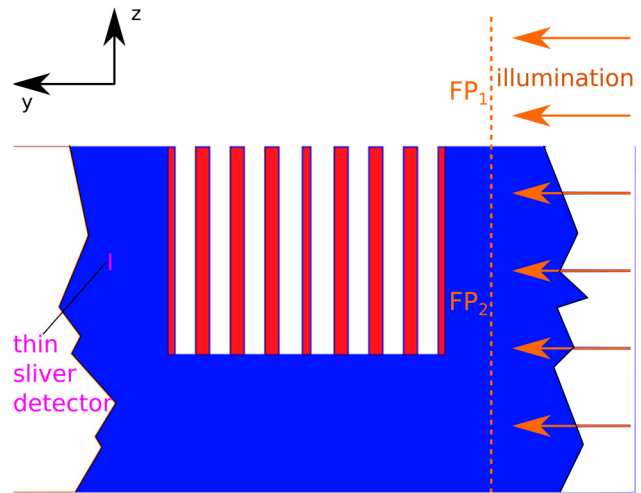


FIG. 19. FDTD detector setup for unbacked, long nanopillar LiPC simulations (side view). The power flux of the light illuminating the system is calculated over a flux plane with nonuniform index.  $FP_1$  has  $n = 1.35$ , whereas  $FP_2$  has  $n = 1.5$ . A thin-sliver detector spanning the  $x$ -direction of the structure is used for calculating transmission through the LiPC.

calculations. For convenience, we consider the structure to be infinitely periodic along the fluid-flow direction ( $x$ -direction).

The 3D FDTD calculation is set up with periodic *Bloch boundary conditions* at the extremities of the fluid-flow direction of the computational cell to represent the periodic nature of the PC, along with perfectly-matched layers (PMLs) at the extremities of

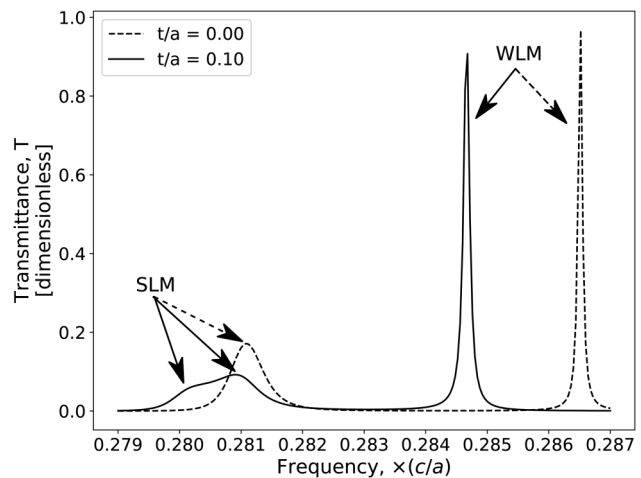
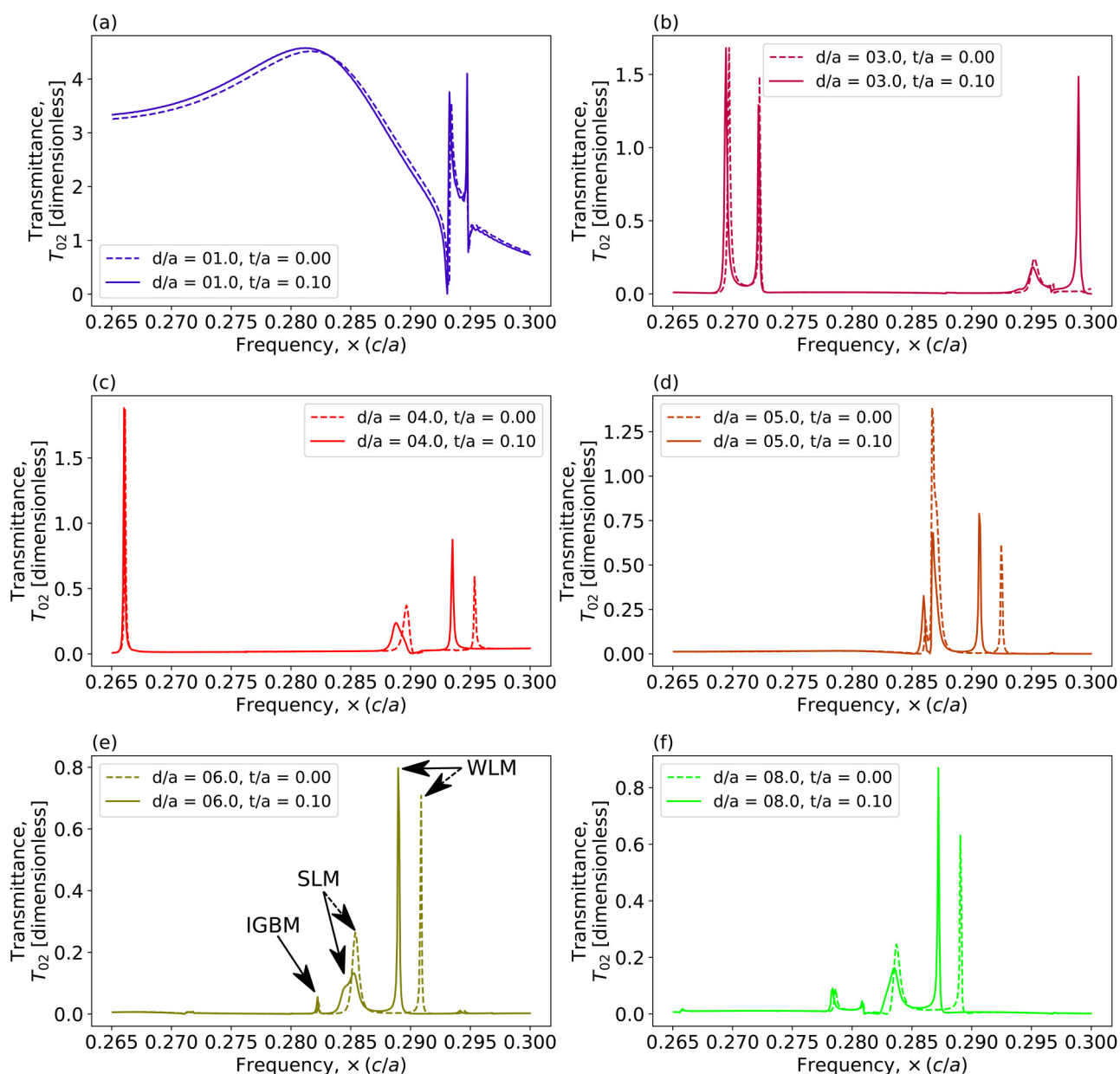


FIG. 20. Transmission spectrum of the 2D progenitor for the WN/WF analyte-binding case with thicknesses  $t/a \in \{0.00, 0.10\}$ . The dashed line indicates the analyte-free case, while the solid line indicates analyte-binding. A redshift occurs with the WLM transmission peak on the right, whereas the SLM peak redshifts, splits into two, while also undergoing transmission-level suppression.

both the light propagation and vertical directions. The optical source is a plane perpendicular to the  $y$ -direction (also referred to as the light propagation direction) such that its edges are a reasonable distance away from the PML terminations. The optical source is vertically polarized, i.e.,  $E(\mathbf{r}, t) = (0, 0, E_z(\mathbf{r}, t))$ .

The intensity (power per unit area) of a light beam with a given dielectric field amplitude is proportional to the refractive

index of the medium it traverses.<sup>36</sup> The planar light source used to illuminate our LiPC cuts through regions with different refractive indices as seen in Fig. 19. Moreover, our thin-slicer detectors for transmitted fluxes involve a different flux plane area from that of the source. We define transmittance using average flux per unit area incident upon the LiPC structures from the light source and the average flux per unit area over the detector slivers.



**FIG. 21.** Nanopillar height optimization for unbacked, long-pillar LiPC design using the WN case of analyte-binding. Various nanopillar heights are investigated for the WN analyte-binding scenario with analyte thicknesses  $t/a \in \{0.00, 0.10\}$ . Transmission spectra are from thin-slicer detectors placed at the midlevel of the nanopillar height for each case. Best replication of 2D paradigm's results is seen for a nanopillar height  $d/a = 6.0$  in (e). SLM, WLM, and IGBM peaks are identified.

Symbolically, for the detector plane sliver  $\mathcal{D}$ , transmittance is calculated as a ratio of Poynting vector fluxes,

$$T_{\mathcal{D}}(\omega) \equiv \frac{\frac{1}{\mathcal{A}_{\mathcal{D}}} \int_{\mathcal{D}} S_y(\omega, \mathbf{r}) d^2\mathbf{r}}{\sum_{\mathcal{G}} \frac{1}{\mathcal{A}_{\mathcal{G}}} \int_{\mathcal{G}} S_y(\omega, \mathbf{r}) d^2\mathbf{r}}. \quad (\text{A1})$$

In Eq. (A1),  $S_y(\omega, \mathbf{r})$  is the spatially-dependent, frequency-domain Poynting vector component in the direction of light propagation,  $\mathcal{G}$  is a set of planar slivers for each refractive-index region cut by the source,  $\mathcal{A}_{\mathcal{D}}$  is the area of the detector plane sliver  $\mathcal{D}$ , and  $\mathcal{A}_{\mathcal{G}}$  is the area of the plane sliver  $\mathcal{G}$ . In the case of Fig. 19,  $\mathcal{D}$  is the single thin-sliver detector, whereas  $\mathcal{G} \in \{FP_1, FP_2\}$ . On the other hand, for the final LiPC geometry in Fig. 3,  $\mathcal{D}$  is any of five thin-sliver detectors labeled by  $\{00, 01, 02, 03, 04\}$  and  $\mathcal{G} \in \{FP_1, FP_2, FP_3, FP_4\}$ . It is entirely possible that for the thin-sliver detectors considered, the area-averaged flux in the numerator in Eq. (A1) exceeds the average incident flux in the denominator. Using this definition of transmittance, values greater than unity are possible. Sliver detectors are necessary for the transmission calculations because the use of a single plane leads to a considerable washing out of the spatial fingerprint of the biomarkers.

In order to establish the optimal nanopillar height  $d$  for the structure in Fig. 18, we first recapture key features of the 2D paradigm's spectral response. In particular, we investigate the case where analyte-binding occurs at  $W$  and one of the  $N$  or  $F$  sites (i.e., for analyte-binding case  $WN/WF$  for the 2D paradigm). For analyte-binding at just one of the two surface gratings, a pure 2D version of the design is oblivious to the distinction between  $N$  and  $F$ .<sup>5</sup> This is no longer true for the LiPC in which there is scattering of light into the third dimension. For reference, we recapitulate the 2D results in Fig. 20, where two values of analyte thickness  $t$  are considered:  $t/a \in \{0.00, 0.10\}$ . There is a transmission peak due to a WLM of the 2D paradigm that redshifts in response to  $WN/WF$  analyte-binding. There is another peak due to the two SLMs visible on the left-hand side of Fig. 20. For analyte-binding involving only one of  $N$  or  $F$ , the SLM peak redshifts and splits into two peaks, with the maximum transmittance levels of the resultant peaks lower than the original single SLM peak.

We now investigate the effect of pillar height  $d$  on the spectral signature of the long nanopillar, glass-backed, open-top system. We explore the full range of the 2D PBG, i.e.,  $0.263 \leq (\omega a)/(2\pi c) \leq 0.326$ , for the  $w = 0.4 \times a$  structure. Figure 21 depicts the effect of progressively larger values of  $d$  on the transmission spectral signature. Transmittance, as defined by Eq. (A1) is not bounded by unity. For small values of  $d$ , such as  $d/a = 1.0$ , the transmission of light is not adequately suppressed in the anticipated PBG region of the PC. Higher values of  $d$  are necessary for the transmission-suppressed PBG signature to emerge. Once this happens, we can distinguish transmission peaks from engineered waveguide and surface modes. The best replication of the transmission signature seen in Fig. 20 occurs at  $d/a = 6.0$ . We also observe that for the LiPC, there are additional transmission peaks in the spectrum.

We point out that in the LiPC systems, the SLMs and WLM corresponding to the 2D counterpart are confined in the  $z$ -direction

(fluid above, glass below) via *index-guiding*. The dependence of these modes on the values of  $d$  is analogous to that of stationary wave normal modes on a string of variable length. The characteristics of the index-guided SLMs and WLMs will match those of the 2D paradigm at particular instances of the pillar height  $d$ . This seems to occur for the first time at  $d/a = 6.0$ , when we observe a reasonably clean replication of the 2D transmission signature. As shown below, the *fundamental mode* of the  $z$ -confined SLM system occurs for  $d/a = 6.0$  in the glass-backed chip, with the same pillar height also close to the necessary value for a WLM fundamental mode.

While it is encouraging to recapture the 2D behavior in our simple LiPC, its long nanopillars may be susceptible to disorder effects. Taller nanopillars are not only difficult to fabricate uniformly and uprightly but are also more prone to damage by fluid flow around them, as well as from nonuniform analyte-binding. This issue is improved in the final design of our LiPC that includes a thin, high-index backing layer between the nanopillars and the glass substrate.

We now compare the spectral signatures of the simplified 2D paradigm and the long nanopillar, glass-backed LiPC. Two things immediately stand out. First, the WLM and SLM peaks in the LiPC [Fig. 21(e)] are blueshifted relative to those of its 2D progenitor (Fig. 20). The extent of this blueshift seems to be progressively reduced by increasing  $d$ . This is analogous to the *Quantum Confinement Effect*, where the *zero-point energy* of a confined wave is increased with increased confinement. Second, additional modes appear in the FSR (presented by the 2D PBG) in the LiPC, while being absent in the pure 2D paradigm. These index-guided modes are supported by the finite  $z$ -extent of the nanopillar array. These index-guided bulk modes (IGBMs) are also valuable for sensing and calibration.

## APPENDIX B: MODE PATTERNS FOR THE UNBACKED, LONG NANOPILLAR LAB-IN-A-PHOTONIC-CRYSTAL

We now consider, in more detail, mode patterns for the  $d/a = 6.0$  case of the glass-backed sensor. We restrict this analysis to the analyte-free case. Representative snapshots for the real part of the electric field, i.e.,  $\Re\{E_z(\mathbf{r}, t)\}$ , for SLM, WLM, and IGBM in the  $t/a = 0$  case are presented in Figs. 22–24, respectively. Two categories of visualizations are presented: one for an  $xy$ -slice of the nanopillars across the  $z$ -midpoints, and the other for  $yz$ -slices of the chip through the  $x$ -centers of the period-doubled PC unit-cells. The spectral locations for the SLM, WLM, and IGBM are shown in Fig. 21(e). The astute reader would observe that IGBM for the long-pillar LiPC corresponds to IGBM1 for its short-pillar counterpart.

Figure 22 shows snapshots of electric field values when illuminating the unbacked  $d/a = 6.0$  system at the SLM transmission peak. It is observed that the SLM is, in fact, a combination of two different surface modes, one antisymmetric about the central waveguide axis—seen in Figs. 22(a)–22(c)—and the other symmetric—seen in Figs. 22(d)–22(f). As seen with particular ease from the  $xy$ -slice of the field maps in Figs. 22(b) and 22(e), the SLM fields have opposite signs on two sides of the  $y$ -axial line (light propagation direction) through the  $x$ -center. Furthermore, based on the  $yz$ -slices

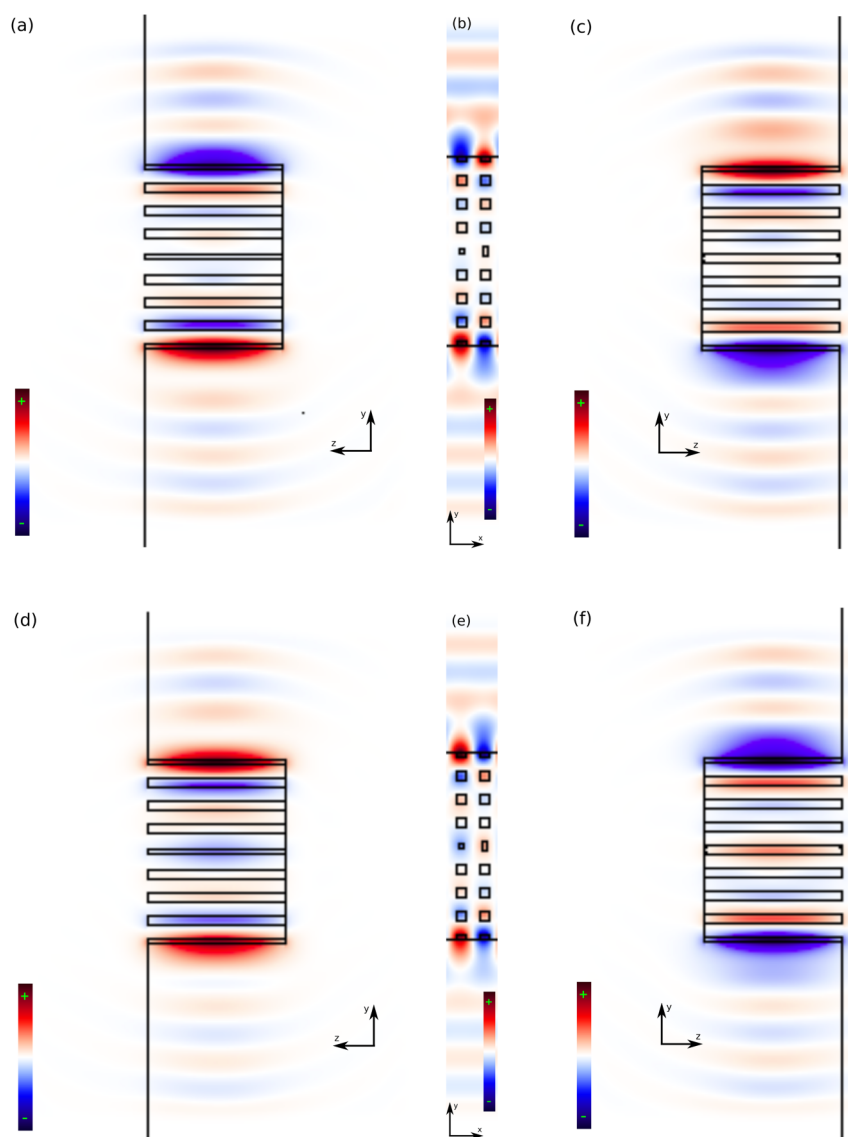


**FIG. 22.** SLM electric field [ $\Re\{E_z\}$ ] snapshots for unbacked, long-pillar LiPC. Two distinct cases are observed—antisymmetric [(a)–(c)] and symmetric [(d)–(f)]; the former admits no field contribution from the waveguide, while the latter does: (a) profile ( $yz$ -slice) of antisymmetric constituent along centerline of left unit-cell of  $x$ -period-doubling, (b) overview ( $xy$ -slice) of antisymmetric constituent at plane through nanopillar  $z$ -centers, (c) profile ( $yz$ -slice) of antisymmetric constituent along centerline of right unit-cell of  $x$ -period-doubling, (d) profile ( $yz$ -slice) of symmetric constituent along centerline of left unit-cell of  $x$ -period-doubling, (e) overview ( $xy$ -slice) of symmetric constituent at plane through nanopillar  $z$ -centers, and (f) profile ( $yz$ -slice) of symmetric constituent along centerline of right unit-cell of  $x$ -period-doubling.

in—seen in Figs. 22(a), 22(c), 22(d), and 22(f)—the SLM is observed to be symmetric about the  $z$ -center of the nanopillars.

We specifically note from Figs. 22(a), 22(c), 22(d), and 22(f) that the  $z$ -confinement of the LiPC SLM is of the *first order*, exhibiting no nodes in this direction. It has peak amplitude at the  $z$ -center and exhibits evanescent decays into the upper (fluid) and lower (glass) regions.

The WLM snapshots in Figs. 23(a)–23(f) for its two constituents are likewise seen to have opposite signs about the  $y$ -axial line (light propagation direction) through the  $x$ -center, while being symmetric about the central-waveguide axis. As apparent from the  $yz$ -slices in Figs. 23(a) and 23(c), the first WLM constituent has peak amplitude at the  $z$ -center, with the majority of the fields localized near the central-waveguide nanopillars. The absence of nodes

in the active region of the sensor in the  $yz$ -slices, illustrated in Figs. 23(a), 23(c), 23(d), and 23(f), suggests  $d/a = 6.0$  to be approximately at the ideal length-scale of the vertically-confined WLM fundamental mode. For the second WLM constituent in Figs. 23(d), 23(e), and 23(f), a noticeable hybridization of the central-waveguide state with a symmetric linear combination of the two surface states is observed. Both WLM constituents exhibit evanescent decay into the surrounding media above and below the active region and correspond to the single peak identified in Fig. 21(e).

In Fig. 24, the field pattern of an index-guided bulk mode (IGBM) is shown for the glass-backed, long nanopillar architecture. From the  $xy$ -slice of the mode in Fig. 24(a), we notice that the fields are spread throughout the bulk of the PC and not restricted

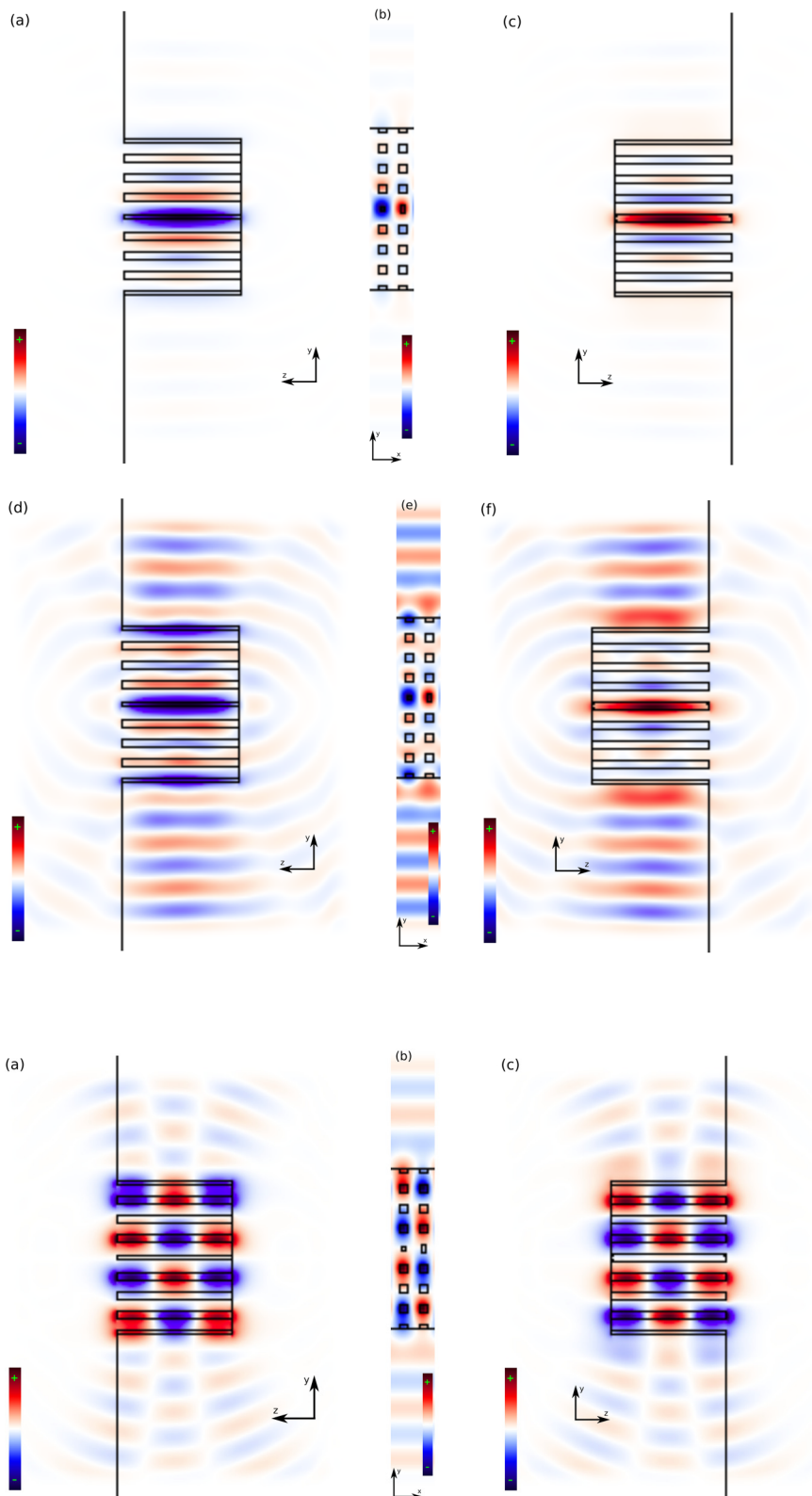


**FIG. 23.** WLM electric field [ $\Re\epsilon(E_z)$ ] snapshots for unbacked, long-pillar LiPC. Two distinct constituents are observed with strong field localization about the waveguide [(a)–(c)] and weak [(d)–(f)]: (a) profile (yz-slice) of first constituent along centerline of left unit-cell of x-period-doubling, (b) overview (xy-slice) of first constituent at plane through nanopillar z-centers, (c) profile (yz-slice) of first constituent along centerline of right unit-cell of x-period-doubling, (d) profile (yz-slice) of second constituent along centerline of left unit-cell of x-period-doubling, (e) overview (xy-slice) of second constituent at plane through nanopillar z-centers, and (f) profile (yz-slice) of second constituent along centerline of right unit-cell of x-period-doubling.

**FIG. 24.** IGBM electric field [ $\Re\epsilon(E_z)$ ] snapshots for unbacked, long-pillar LiPC. (a) Profile (yz-slice) along centerline of left unit-cell of x-period-doubling, (b) overview (xy-slice) at plane through nanopillar z-centers, and (c) profile (yz-slice) along centerline of right unit-cell of x-period-doubling.

to the central waveguide or surface gratings. The two-node pattern in the  $z$ -direction in Fig. 24(b) suggests that this is a third-order vertically-confined mode of the finite-height PC structure. We anticipate the presence of other IGBMs at different frequencies within the LiPC.

It should be emphasized that the IGBMs do not encumber the SLM and WLM functionalities needed for biosensing. In other words, we still retain a sufficient FSR in Fig. 21(e) for the SLM and WLM interactions to proceed largely unaffected by the set of IGBMs that emerge due to finiteness in the vertical direction. It was shown earlier that IGBMs can provide valuable calibration for the LiPC.

## APPENDIX C: DESIGN PRINCIPLES FOR BACKED, SHORT NANOPILLAR LAB-IN-A-PHOTONIC-CRYSTAL

### 1. High-index backing layer selection

In order to reduce nanopillar heights while retaining the full functionality of our LiPC, we introduce a *thin* backing layer of a high-index material between the nanopillars and the glass substrate. The resulting higher overall refractive index in the active region causes a smaller proportion of the electromagnetic fields to leak into the fluid region above the chip and the glass region below. On the other hand, an overly thick layer of a high-index material may affect the vital sensing modes in an undesirable way. Ideally, this high-index backing should be tailored to create only a *small* perturbation to the mode structure of the previous glass-backed, vertically-protruded LiPC. Also, any additional modes introduced by the backing layer should not interact with the previously-identified sensing modes. Accordingly, we introduce a thin, high-index ( $n = 3.4$ ) material of thickness  $b$  (Fig. 1) and investigate the resulting spectral signature for various choices of nanopillar height  $d$ . We also consider a variety of combinations for  $b$  and  $d$  values with a view to recapturing the spectral response of the 2D progenitor<sup>5</sup> to analyte-binding. We aim to minimize the required value of  $d$ .

Iterating over a number of high-index backing thicknesses,  $b/a \in \{0.1, 0.2, 0.3\}$ , results for the  $d/a = 3.0$  case are presented in Fig. 25. For ease of reading, we postpone results for  $d/a \in \{1.0, 2.0, 4.0\}$  to Appendix C 2. The best overall spectral response is found for  $b/a = 0.2$  and  $d/a = 3.0$ . This is a reduction of the nanopillar height by *half* from the long-pillar LiPC.

We observe from Fig. 25 that for  $b/a > 0.2$ , there is a significant cluttering of the spectrum by optical modes introduced by the high-index backing material itself. On the other hand, for  $b/a = 0.1$ , the SLM peak is impinged upon by an index-guided bulk mode, labeled IGBM1 in Fig. 25(a). We also observe the presence of a second IGBM, labeled IGBM2. Fortunately, the conflict between IGBM1 and SLM seen for  $b/a = 0.1$  is ameliorated for  $b/a = 0.2$ . We notice a redshift of the modes in Fig. 25(b) relative to 25(a) due to a larger overall index of the structure with a thicker high-index backing material. The confinement lengths are the same for both systems. We also note that due to the smaller  $d$  values in Fig. 25(b), the relevant modes are blueshifted relative to those of the long nanopillar device in Fig. 21(e). This is a manifestation of stronger wave-localization effects for the short-pillar LiPC.

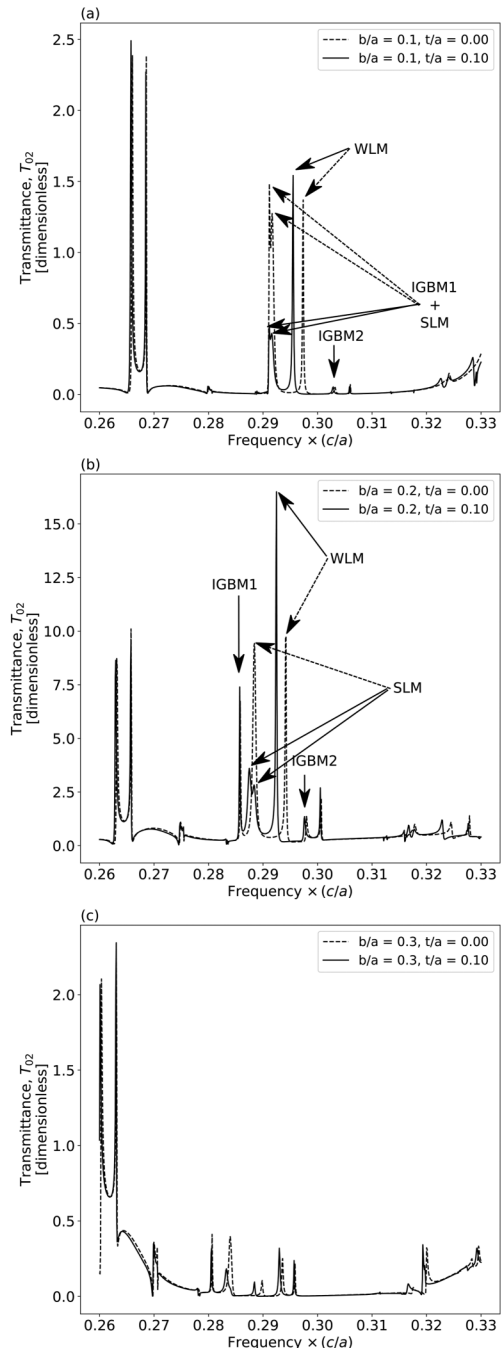


**FIG. 25.** Transmittance data at detector O2 for various high-index backing thicknesses for the short-pillar LiPC ( $d/a = 3.0$ ). (a)  $b/a = 0.1$ : there are two IGBM peaks—IGBM1 lies near SLM and IGBM2 near WLM. IGBM1 and SLM infringe upon each other. (b)  $b/a = 0.2$ : again, two IGBM peaks are seen—IGBM1 is near SLM and IGBM2 near WLM. IGBM1 is well separated from SLM. The overall signal-to-noise ratio is also better for this configuration, as indicated by the significantly higher transmittance levels. (c)  $b/a = 0.3$ : for  $b/a > 0.2$ , the backing material is too thick for functionality.

## 2. Nanopillar height selection

Here, we present additional results for the optimization of nanopillar height  $d$  and high-index backing thickness  $b$  for the LiPC design. Data for  $b$ -optimization for the  $d/a = 3.0$  case has already been presented in Fig. 25. Results from the spectral calculations for  $d/a$  values of 1.0, 2.0, and 4.0 are presented in Figs. 26, 27, and 28, respectively.

In the case of a short protrusion with  $d/a = 1.0$ , edges of the 2D PBG are poorly delineated. There is some indication of SLM formation, as evidenced by its peak-splitting behavior in Fig. 26(a) in response to analyte-binding at one of the two surface gratings. The SLM and WLM peaks in Figs. 26(b) and 26(c) are already infringed by the malformed upper edges of the 2D PBG. For  $b/a > 0.3$ , the system does not admit any modes well-adapted to sensing. Overall, the value  $d/a = 1.0$  is unsuitable for a functional LiPC. We also note that the SLM and WLM frequencies are strongly blueshifted relative to those of the final LiPC design. This is due to the significantly stronger confinement effect with thick backing and very small nanopillar height. Furthermore, for such small  $d$ , the SLM and WLM frequencies in Figs. 26(a), 26(b), and 26(c) exhibit significant susceptibility to small changes in  $b$ .

For  $d/a = 2.0$ , rudimentary SLM and WLM signatures are visible for  $b/a \in \{0.1, 0.2\}$  in Figs. 28(a) and 28(b). Once again, the SLM and WLM frequencies are blueshifted relative to the  $d/a = 3.0$  case. The desired behavior of the 2D prototype is not replicated, and the transmission spectrum worsens with increasing  $b$ , as seen in Fig. 28(c). This  $d$  is also unsuitable for biosensing. Relative to the  $d/a = 1.0$  case, the longer nanopillars with  $d/a = 2.0$  make the SLM and WLM resonance frequencies in Figs. 27(a) and 27(b) less susceptible to changes in  $b$ .

For the case of  $d/a = 4.0$ , there are traces of SLM and WLM behavior for  $b/a \in \{0.1, 0.2\}$  in Figs. 28(a) and 28(b) and of a poorly-formed SLM for  $b/a = 0.3$  in Fig. 28(c). Furthermore, the SLM in Fig. 28(b) is too close to an IGBM, rendering the system dysfunctional. The spectral characteristics deteriorate further for larger values of  $b$ , as seen in Fig. 28(c). Overall, a better spectrum has already been observed for smaller  $d$ .

Both  $d/a = 5.0$  and  $d/a = 6.0$  are found to be poor choices for the LiPC design due to extensive spectral clutter. While it is possible to discern WLM and SLM resonances in some cases, shorter nanopillars yield better spectral fingerprints. Optimal values for the LiPC design consist of nanopillars with height  $d/a = 3.0$  and a high-index-backing layer thickness  $b/a = 0.2$ .

## 3. Notes on the final pillar height for the short nanopillar lab-in-a-photonic-crystal

Further insight into the SLM, WLM, and IGBM1 field maps for the backed short nanopillar LiPC is obtained from the vertical component of the Poynting vector,  $S_z$ , for corresponding modes in the unbacked, long nanopillar LiPC shown in Fig. 29. For each of the three modes,  $S_z$  is seen to be antisymmetric about the dashed horizontal plane slicing through the middle of the long pillars. This nodal plane for  $S_z$  readily accommodates a thin ( $b/a = 0.2$ ) high-index sheet with minimal disturbance of the upper half of the SLM, WLM, and IGBM1 patterns. For a marginally thicker high-index backing, these modes are altered significantly, leading to the compromised transmission spectra in Fig. 25(c).

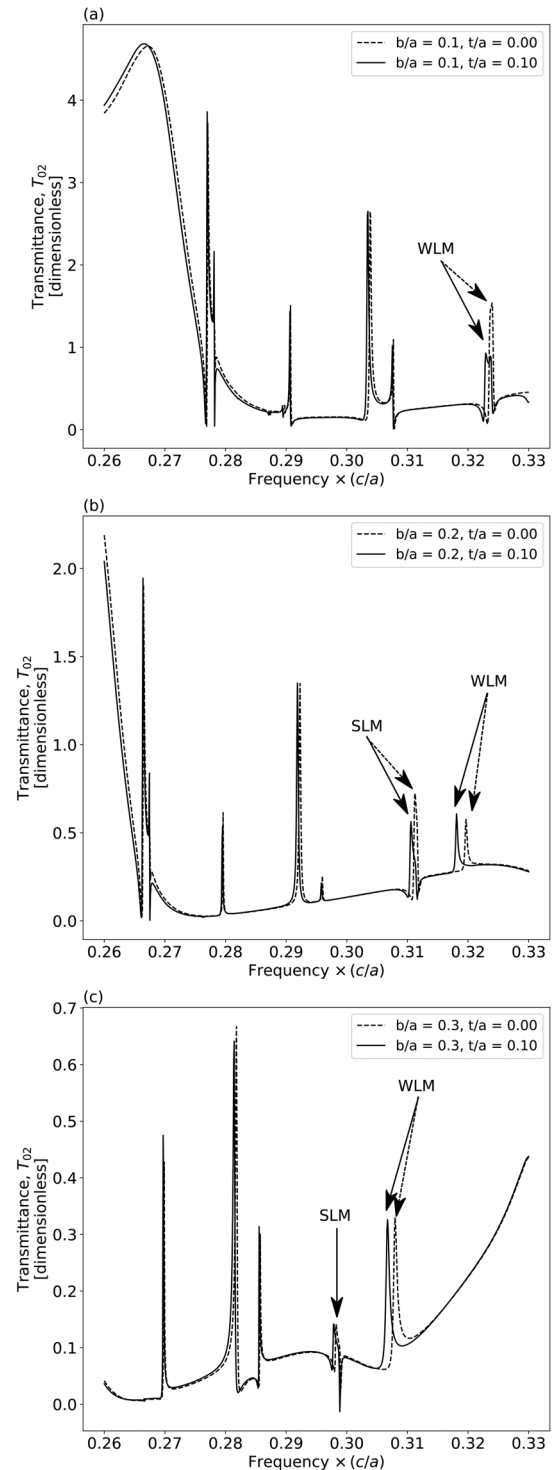


**FIG. 26.** Spectral data for various high-index backing thicknesses for the case  $d/a = 1.0$ . (a), (b), (c) correspond to  $b/a \in \{0.1, 0.2, 0.3\}$ , respectively, for transmittance in silver detector 02.

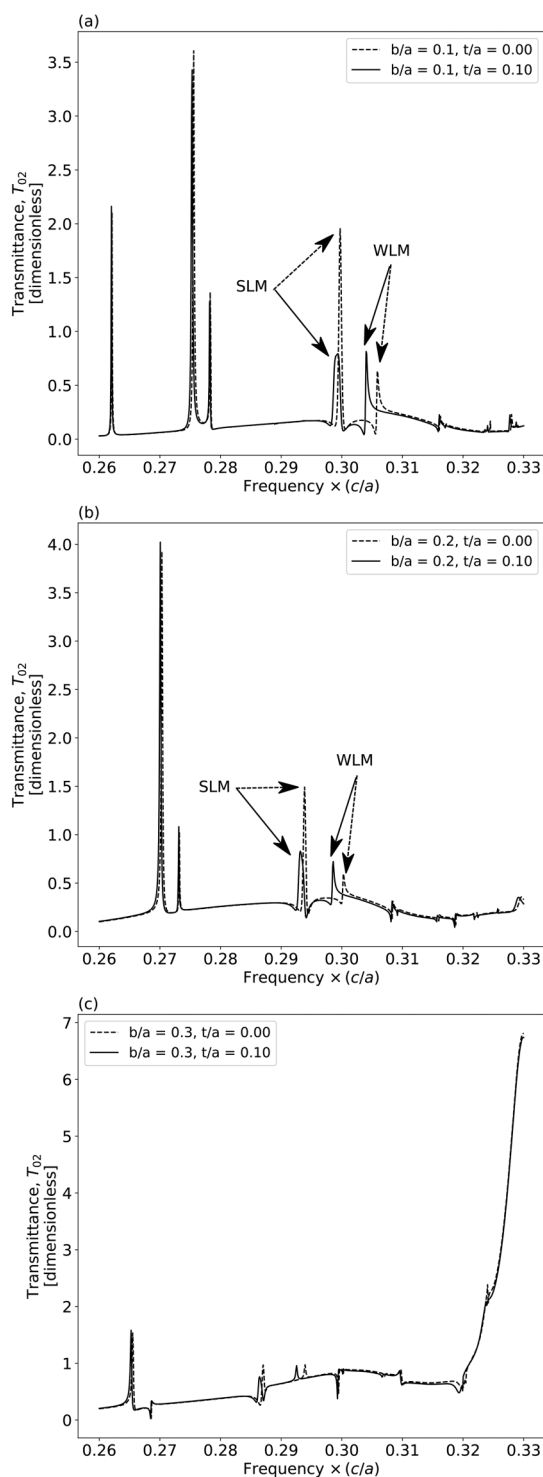


**FIG. 27.** Spectral data for various high-index backing thicknesses for the case  $d/a = 2.0$ . (a), (b), (c) correspond to  $b/a \in \{0.1, 0.2, 0.3\}$ , respectively, for transmittance in sliver detector 02.

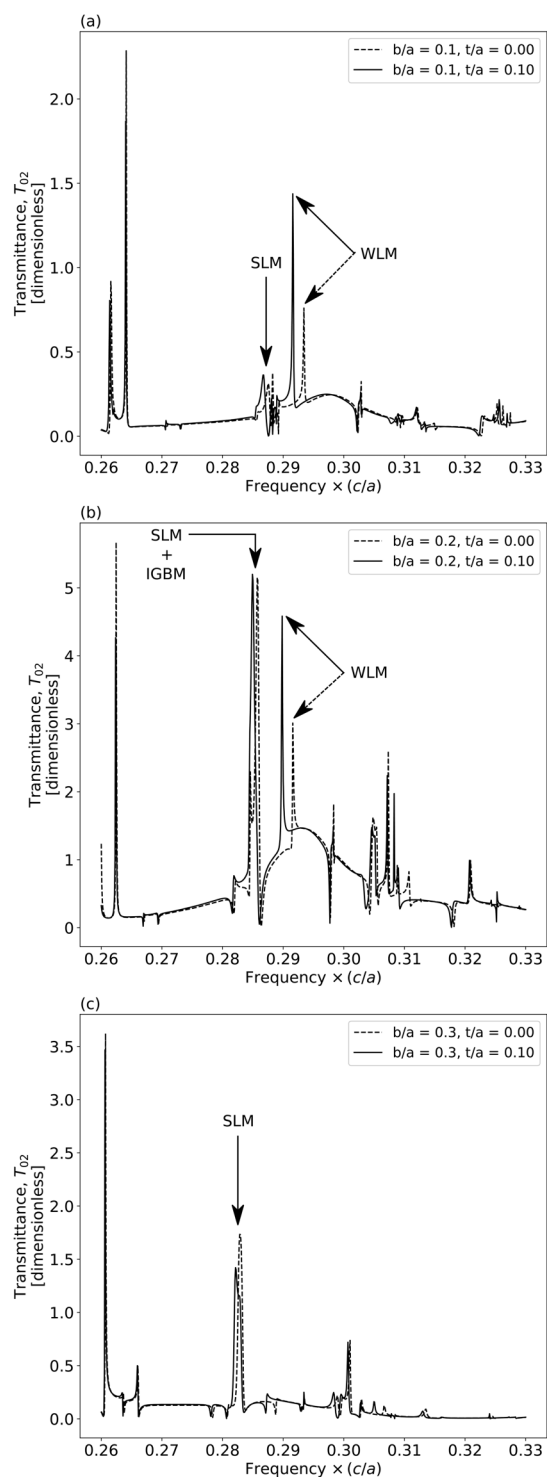


**FIG. 28.** Spectral data for various high-index backing thicknesses for the case  $d/a = 4.0$ . (a), (b), (c) correspond to  $b/a \in \{0.1, 0.2, 0.3\}$ , respectively, for transmittance in sliver detector 02.

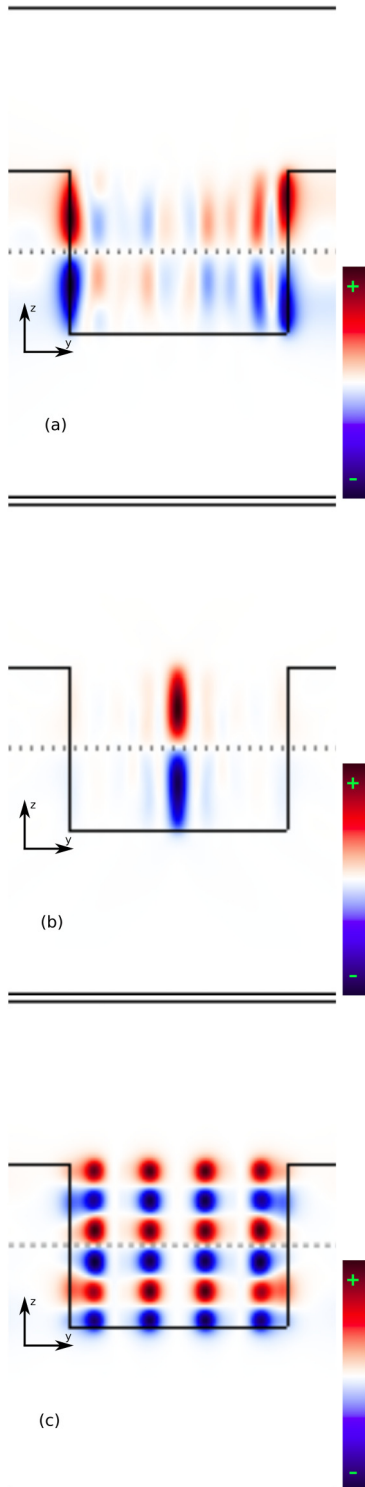


**FIG. 29.** Profile view of Poynting vector field ( $S_z$ ) snapshots for unbacked, long-pillar LiPC. (a) SLM, (b) WLM, (c) IGBM1.

**APPENDIX D: DIELECTRIC CONSTANT AVERAGING FOR FINITE-DIFFERENCE TIME-DOMAIN CALCULATIONS**

In order to keep repetitive 3D calculations tractable, a low spatial resolution of 10 mesh points per PC unit-cell length is used. To retain a more accurate representation of the detailed architecture, the dielectric constant,  $\epsilon$ , at each mesh point is approximated as an average over a  $10 \times 10 \times 10$  subgrid. This is implemented as a special feature in C++ version of *Meep*.

For simplicity, spatial averaging of the dielectric constant,  $\epsilon$ , for our FDTD calculations is illustrated conceptually using a simplified 2D geometry. Spatial approximations are exaggerated in the diagrams for clarity. In Fig. 30(a), a circular area of dielectric material is visualized on a grid for FDTD calculations. Each large square represents the area covered by a single FDTD mesh point. Jagged edges due to the discretization of space are visible. A dashed outline depicts the original circle. The creation of a coarse-grained version of the geometry by spatial averaging over a fine  $5 \times 5$  subgrid of points within each FDTD mesh is shown. The FDTD coarse-grained mesh points lie at the centers of the squares outlined by the thicker rulings on the grid.

The resultant  $\epsilon$ -averaged dielectric profile is depicted in Fig. 30(b). The dielectric constant,  $\epsilon$ , at a coarse-grained mesh point is taken to be the *arithmetic mean* of the values in the  $5 \times 5$  subgrid. Visually, the coarse-grained profile no longer resembles a circle in this exaggerated illustration. With dilution of the  $\epsilon$  values at the edges, the optical response of the dielectric circle is approximately retained. However, the alignment of the coarse-grained grid and the actual structure has some effect on the approximate geometry. We benchmark our  $\epsilon$ -averaged representation against full-blown high-resolution FDTD simulations. While designing the LiPC, the  $\epsilon$ -averaging scheme greatly reduces the 3D simulation time. For the 2D progenitor geometry, we find reasonable agreement with calculations involving a linear resolution four times higher. Only slight variations of resonant frequencies and frequency-shifts are observed. In addition to reducing the simulation time, the spatially coarse-grained FDTD calculation provides an indication of robustness of the spectral fingerprints to random imperfections of a similar spatial magnitude.

**APPENDIX E: DETAILED PERFORMANCE CURVES FOR HIGH-INDEX-BACKED LAB-IN-A-PHOTONIC-CRYSTAL**

We now turn to quantitatively characterizing the sensing properties of the short nanopillar LiPC. In particular, we fit the individual peaks in the spectral data using an *asymmetric Lorentzian function*

$$\mathcal{Q}_{asym,p}(\omega) \equiv \begin{cases} \frac{A_p}{\left[1 + \left(\frac{\omega - \omega_{0,p}}{\omega_{s,p}}\right)^2\right]^{L_p}} & \omega \leq \omega_{0,p}, \\ \frac{A_p}{\left[1 + \left(\frac{\omega - \omega_{0,p}}{\omega_{s,p}}\right)^2\right]^{R_p}} & \omega > \omega_{0,p}. \end{cases} \quad (E1)$$

For the  $p$ th peak,  $A_p$  is the maximum transmittance,  $\omega_{0,p}$  is the center frequency,  $\omega_{s,p}$  is the Lorentzian frequency width, while  $L_p$  and  $R_p$  are asymmetrical shape parameters. We model the transmission spectra as a summation over up to four asymmetric

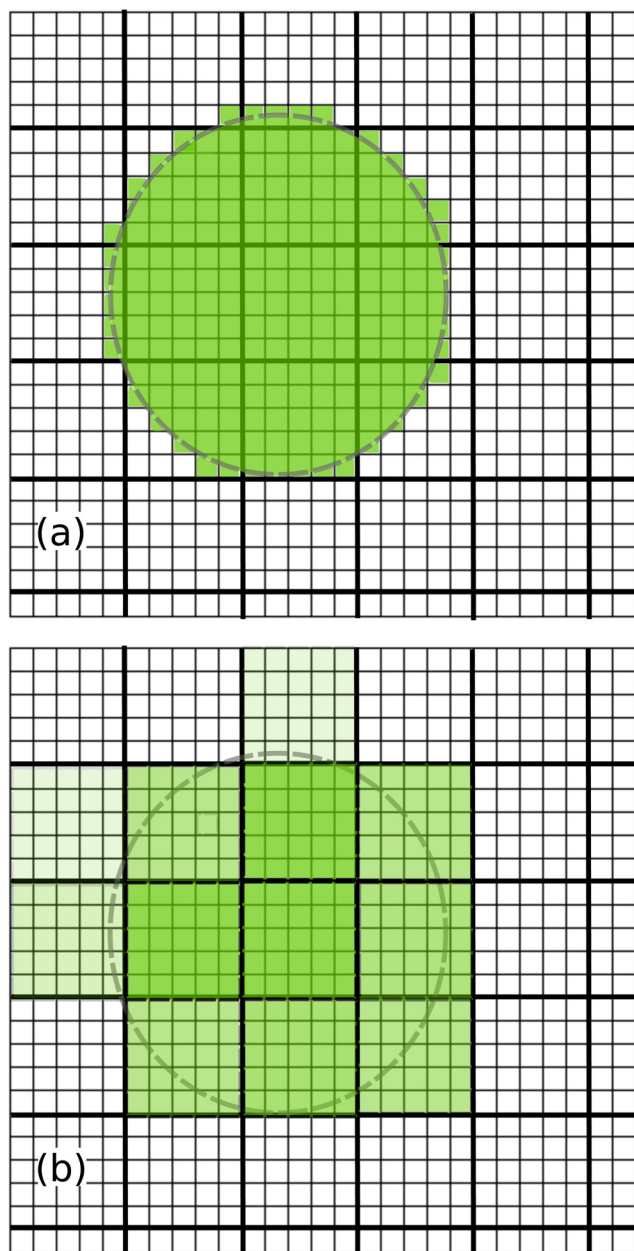


**FIG. 30.** Illustration of dielectric-profile averaging using a circle. (a) Fine-grained representation: centers of squares formed by the lighter rulings on the grid represent the  $\epsilon$ -averaging mesh, whereas centers of squares formed by the darker rulings form the actual FDTD mesh. A dashed outline of the original circle is shown for reference, along with the jagged edges due to the discretization of space. (b) Coarse-grained representation: centers of squares formed by the thicker rulings on the grid represent the coarse FDTD mesh. The value of  $\epsilon$  at each coarse-grained mesh point is an arithmetic mean over the  $5 \times 5$  subgrid spanned. Various levels of  $\epsilon$ -“smearing” occur at the interface of the circle with the surrounding medium, resulting in a geometry that may fail to resemble a circle visually, but should recapture light-scattering behavior from a circle in a less exaggerated case than illustrated.

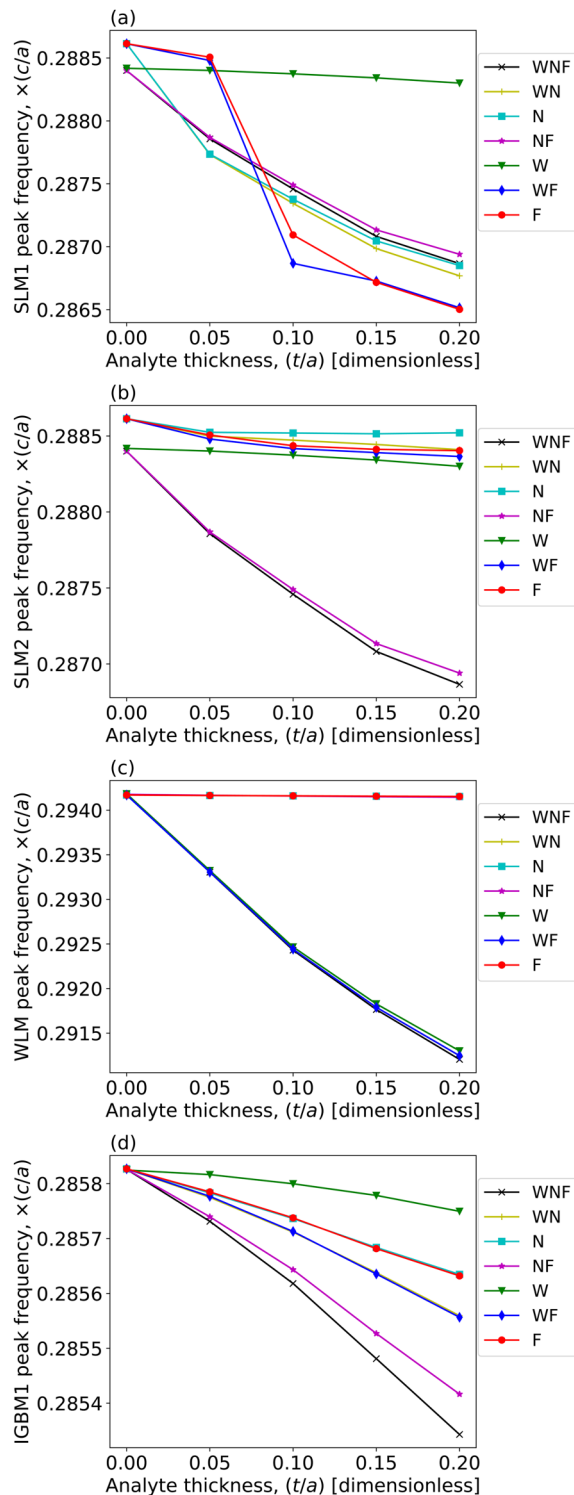


**FIG. 31.** Calibration curves for transmission peak frequencies of the backed, short-pillar LiPC. (a) SLM1, (b) SLM2, (c) WLM, and (d) IGBM1.

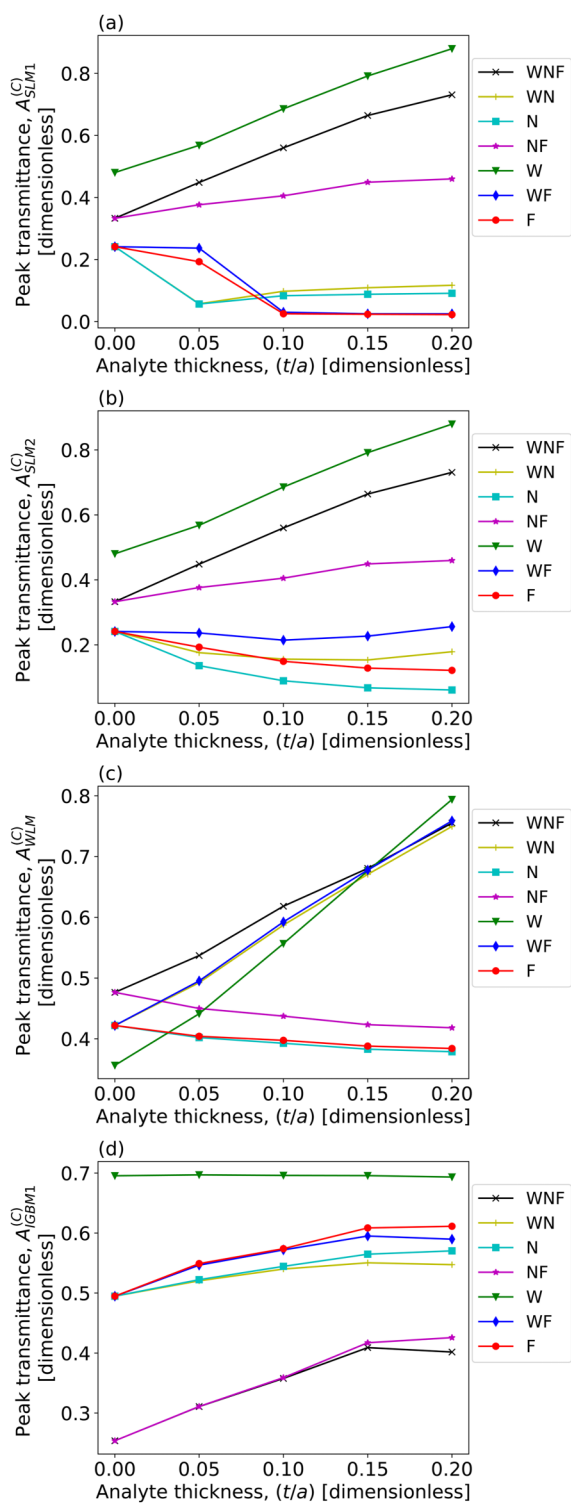


FIG. 32. Calibration curves for transmission peak levels of the backed, short-pillar LiPC. (a) SLM1, (b) SLM2, (c) WLM, and (d) IGBM1.

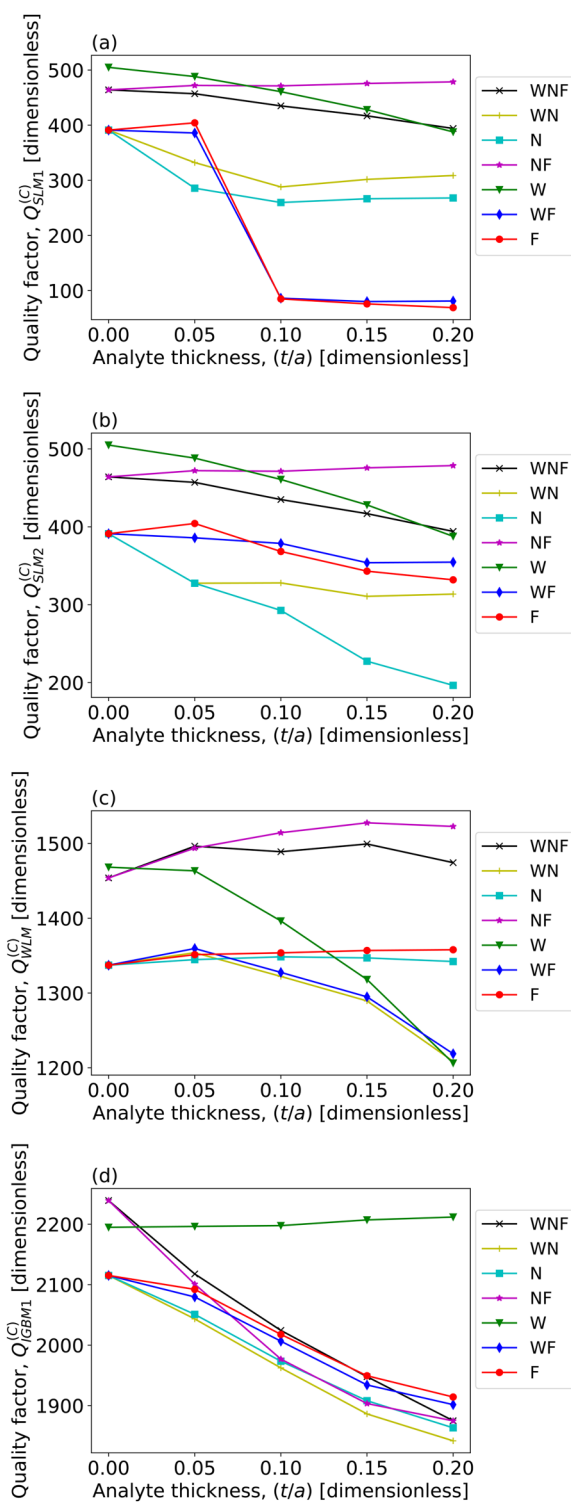


FIG. 33. Calibration curves for quality factors of the backed, short-pillar LiPC. (a) SLM1, (b) SLM2, (c) WLM, and (d) IGBM1.

Lorentzian functions, corresponding to the four observed peaks for IGBM1, SLM (up to two peaks), and WLM. In other words,

$$T(\omega) = \sum_p \mathcal{L}_{asym,p}(\omega). \quad (\text{E2})$$

For the  $p$ th peak, the  $Q$  factor is calculated as the ratio of the center frequency to the full width at half maximum, resulting in the following relation:

$$Q_p = \frac{\omega_{0,p}}{\omega_{s,p} \left( \sqrt{2^{1/L_p} - 1} + \sqrt{2^{1/R_p} - 1} \right)}. \quad (\text{E3})$$

We use Eq. (E2) to fit the spectral data in Figs. 8(a), 9(b), 10(b), 11(b), 12(b), 13(a), and 14(a). SciPy package<sup>37</sup> in the Python programming language is leveraged for performing *Least Squares Fitting* of the data. More specifically, for analyte-binding cases  $C \in \{W, N, WN, F, WF, NF, WNF\}$ , there are up to four peaks  $p \in \{IGBM1, SLM1, SLM2, WLM\}$  to be used for the data fitting. The fitted mode frequencies,  $\omega_{0,p}^{(C)}(t/a)$ , are plotted in Fig. 31 for various  $p$  and  $C$  cases. Obviously, these fitted values are functions of the normalized analyte thickness,  $t/a$ . From the same data-fitting operations, the peak transmittance values  $A_p^{(C)}(t/a)$  are plotted in Fig. 32. Lastly, for completeness, we include results for  $Q_p^{(C)}(t/a)$ —calculated via Eq. (E3) (Fig. 33).

## REFERENCES

- E. Yablonovitch, "Inhibited spontaneous emission in solid-state physics and electronics," *J. Phys. Rev. Lett.* **58**, 2059–2062 (1987).
- S. John, "Strong localization of photons in certain disordered dielectric superlattices," *J. Phys. Rev. Lett.* **58**, 2486–2489 (1987).
- J. N. Winn, R. D. Meade, and J. Joannopoulos, "Two-dimensional photonic band-gap materials," *J. Mod. Opt.* **41**, 257–273 (1994).
- R. D. Meade, K. D. Brommer, A. M. Rappe, and J. D. Joannopoulos, "Electromagnetic Bloch waves at the surface of a photonic crystal," *Phys. Rev. B* **44**, 10961–10964 (1991).
- A. Al Rashid and S. John, "Optical biosensing of multiple disease markers in a photonic-band-gap lab-on-a-chip: A conceptual paradigm," *Phys. Rev. Appl.* **3**, 034001-1–034001-9 (2015).
- Y. Zou, S. Chakravarty, L. Zhu, and R. T. Chen, "The role of group index engineering in series-connected photonic crystal microcavities for high density sensor microarrays," *Appl. Phys. Lett.* **104**, 141103 (2014).
- H. Yan, C.-J. Yang, N. Tang, Y. Zou, S. Chakravarty, A. Roth, and R. T. Chen, "Specific detection of antibiotics by silicon-on-chip photonic crystal biosensor arrays," *IEEE Sens. J.* **17**, 5915–5919 (2017).
- University of Texas, in *Automatic Silicon Nanomembrane-based Early Cancer Detection System Demonstrated at SPIE Photonics West Conference* (University of Texas, 2019).
- M. R. Lee and P. M. Fauchet, "Two-dimensional silicon photonic crystal based biosensing platform for protein detection," *J. Opt. Express* **15**, 4530–4535 (2007).
- E. Chow, A. Grot, L. W. Mirkarimi, M. Sigalas, and G. Girolami, "Ultra-compact biochemical sensor built with two-dimensional photonic-crystal microcavity," *Opt. Lett.* **29**, 1093–1095 (2004).
- N. Skivesen, A. Tétu, M. Kristensen, J. Kjems, L. H. Frandsen, and P. I. Borel, "Photonic-crystal waveguide biosensor," *Opt. Express* **15**, 3169–3176 (2007).
- V. N. Konopsky and E. V. Alieva, "Photonic crystal surface waves for optical biosensors," *Anal. Chem.* **79**, 4729–4735 (2007).
- J. Homola, S. S. Yee, and G. Gauglitz, "Surface plasmon resonance sensors: Review," *Sens. Actuators B Chem.* **54**, 3–15 (1999).
- C. Wu, N. Arju, G. Kelp, J. A. Fan, J. Dominguez, E. Gonzales, E. Tutuc, I. Brener, and G. Shvets, "Spectrally selective chiral silicon metasurfaces based on infrared Fano resonances," *Nat. Commun.* **5**, 3892 (2014).
- B. T. Cunningham, P. Li, S. Schulz, B. Lin, C. Baird, J. Gerstenmaier, C. Genick, F. Wang, E. Fine, and L. Laing, "Label-free assays on the BIND system," *J. Biomol. Screen.* **9**, 481–490 (2004).
- H. Cai, M. A. Stott, D. Ozcelik, J. W. Parks, A. R. Hawkins, and H. Schmidt, "On-chip wavelength multiplexed detection of cancer DNA biomarkers in blood," *J. Biomed. Opt.* **10**, 064116 (2016).
- J. Vörös, J. Ramsden, G. Csucs, I. Szendrői, S. De Paul, M. Textor, and N. Spencer, "Optical grating coupler biosensors," *Biomaterials* **23**, 3699–3710 (2002).
- Y. Fang, "Label-free cell-based assays with optical biosensors in drug discovery," *J. Assay Drug Dev. Technol.* **4**, 583–595 (2006).
- Y. Fang, A. M. Ferrie, N. H. Fontaine, J. Mauro, and J. Balakrishnan, "Resonant waveguide grating biosensor for living cell sensing," *Biophys. J.* **91**, 1925–1940 (2006).
- S. Feng, J.-H. Jiang, A. Al Rashid, and S. John, "Biosensor architecture for enhanced disease diagnostics: Lab-in-a-photonic-crystal," *Opt. Express* **24**, 12166–12191 (2016).
- N. Mortensen, S. Xiao, and J. Pedersen, "Liquid-infiltrated photonic crystals: Enhanced light-matter interactions for lab-on-a-chip applications," *Microfluid. Nanofluidics* **4**, 117–127 (2008).
- M. El-Beheiry, V. Liu, S. Fan, and O. Levi, "Sensitivity enhancement in photonic crystal slab biosensors," *Opt. Express* **18**, 22702–22714 (2010).
- T. Xu, N. Zhu, M. Y.-C. Xu, L. Wosinski, J. S. Aitchison, and H. Ruda, "Pillar-array based optical sensor," *Opt. Express* **18**, 5420–5425 (2010).
- J. Vörös, "The density and refractive index of adsorbing protein layers," *Biophys. J.* **87**, 553–561 (2004).
- M. Liss, B. Petersen, H. Wolf, and E. Prohaska, "An aptamer-based quartz crystal protein biosensor," *Anal. Chem.* **74**, 4488–4495 (2002).
- V. Pavlov, Y. Xiao, B. Shlyahovskiy, and I. Willner, "Aptamer-functionalized Au nanoparticles for the amplified optical detection of thrombin," *J. Am. Chem. Soc.* **126**, 11768–11769 (2004).
- M. Huang, A. A. Yanik, T.-Y. Chang, and H. Altug, "Sub-wavelength nanofluidics in photonic crystal sensors," *J. Opt. Express* **17**, 24224–24233 (2009).
- M. L. Adams, M. Loncar, A. Scherer, and Y. Qiu, "Microfluidic integration of porous photonic crystal nanolasers for chemical sensing," *IEEE J. Sel. Area Commun.* **23**, 1348–1354 (2005).
- L. Golobokova, Y. V. Nastaushchev, F. Dultsev, D. Gulyaev, A. Talochkin, and A. Latyshev, "Fabrication and optical properties of silicon nanopillars," *J. Phys. Conf. Ser.* **541**, 012074 (2014).
- Y.-F. Chang, Q.-R. Chou, J.-Y. Lin, and C.-H. Lee, "Fabrication of high-aspect-ratio silicon nanopillar arrays with the conventional reactive ion etching technique," *Appl. Phys. A* **86**, 193–196 (2007).
- W. Li, L. Xu, W.-M. Zhao, P. Sun, X.-F. Huang, and K.-J. Chen, "Fabrication of large-scale periodic silicon nanopillar arrays for 2d nanomold using modified nanosphere lithography," *J. Appl. Surf. Sci.* **253**, 9035–9038 (2007).
- Q. Gao, D. Saxena, F. Wang, L. Fu, S. Mokkaapati, Y. Guo, L. Li, J. Wong-Leung, P. Caroff, H. H. Tan *et al.*, "Selective-area epitaxy of pure wurtzite InP nanowires: High quantum efficiency and room-temperature lasing," *Nano. Lett.* **14**, 5206–5211 (2014).
- J. A. Lewis and G. M. Gratson, "Direct writing in three dimensions," *J. Mater. Today* **7**, 32–39 (2004).
- J. R. Raney and J. A. Lewis, "Printing mesoscale architectures," *MRS Bull.* **40**, 943–950 (2015).
- A. F. Oskooi, D. Roundy, M. Ibanescu, P. Bermel, J. Joannopoulos, and S. G. Johnson, "MEEP: A flexible free-software package for electromagnetic simulations by the FDTD method," *J. Comput. Phys. Commun.* **181**, 687–702 (2010).
- B. E. Saleh, M. C. Teich, and B. E. Saleh, *Fundamentals of Photonics* (Wiley, New York, 1991), Vol. 22.
- E. Jones, T. Oliphant, P. Peterson *et al.*, "SciPy: open source scientific tools for Python" (2001).